

ARTICLE

Open Access

Adenosine-independent regulation of the sleep–wake cycle by astrocyte activity

Wanling Peng^{1,2}✉, Xiaotong Liu^{1,2}, Guofen Ma^{3,4}, Zhaofa Wu^{5,6}, Ziyue Wang^{3,4}, Xiang Fei^{1,2}, Meiling Qin¹, Lizhao Wang^{3,4}, Yulong Li^{5,6,7}✉, Siyu Zhang^{3,4}✉ and Min Xu^{1,2,8}✉

Abstract

Astrocytes play a crucial role in regulating sleep–wake behavior, and adenosine signaling is generally thought to be involved. Here we show multiple lines of evidence supporting that modulation of the sleep–wake behavior by astrocyte Ca^{2+} activity could occur without adenosine signaling. In the basal forebrain and the brainstem, two brain regions that are known to be essential for sleep–wake regulation, chemogenetically-induced astrocyte Ca^{2+} elevation significantly modulated the sleep–wake cycle. Although astrocyte Ca^{2+} level positively correlated with the amount of extracellular adenosine, as revealed by a genetically encoded adenosine sensor, we found no detectable change in adenosine level after suppressing astrocyte Ca^{2+} elevation, and transgenic mice lacking one of the major extracellular ATP-adenosine conversion enzymes showed similar extracellular adenosine level and astrocyte Ca^{2+} -induced sleep modulation. Furthermore, astrocyte Ca^{2+} is dependent primarily on local neuronal activity, causing brain region-specific regulation of the sleep–wake cycle. Thus, neural activity-dependent astrocyte activity could regulate the sleep–wake behavior independent of adenosine signaling.

Introduction

Astrocytes are one of the most abundant cell types in the brain¹. They provide essential support to the neural network and actively participate in many brain functions, including sleep–wake regulation^{2–6}. Astrocytes have been proposed to modulate the sleep–wake cycle through multiple mechanisms⁷, among which adenosine signaling is generally believed to be critical^{3,8}. Astrocyte-derived adenosine, produced by the hydrolysis of astrocyte-released ATP, was shown to regulate slow cortical oscillations⁹ and control the accumulation of sleep pressure^{8,10}. In these studies, astrocyte-specific exocytosis was inhibited by expressing the dominant-negative domain of

vesicular SNARE (dnSNARE) that was driven by the glial-fibrillary acidic protein (GFAP) promoter¹¹.

In the dnSNARE mice, the involvement of astrocyte-derived adenosine in the sleep–wake regulation was indirectly validated via pharmacological blockade of adenosine receptors, and no direct measurement of extracellular adenosine level was performed, mainly due to the lack of sensitive tools to measure adenosine level in live animals. Additionally, the constitutive GFAP promoter used in these studies to achieve astrocyte-specific transgene expression has been shown to be not specific to astrocytes but also lead to considerable leaky expression in neurons^{12–14}. These methodological concerns raise an important question of whether astrocyte-derived adenosine plays a critical role in sleep–wake regulation.

Extracellular adenosine can originate from ATP hydrolysis or equilibrative nucleoside transporter (ENT)-mediated release¹⁵. Both astrocytes and neurons have been implicated in these processes¹⁵, although their relative contribution is unclear. Our recent measurement of neuronal activity-dependent fast adenosine release in

Correspondence: Wanling Peng (wlpeng@ion.ac.cn) or Siyu Zhang (zhang_siyu@sjtu.edu.cn) or Min Xu (mxu@ion.ac.cn)

¹Institute of Neuroscience, State Key Laboratory of Neuroscience, CAS Center for Excellence in Brain Science and Intelligence Technology, Chinese Academy of Sciences, Shanghai, China

²University of Chinese Academy of Sciences, Beijing, China

Full list of author information is available at the end of the article

These authors contributed equally: Wanling Peng, Xiaotong Liu, Guofen Ma

© The Author(s) 2023



Open Access This article is licensed under a Creative Commons Attribution 4.0 International License, which permits use, sharing, adaptation, distribution and reproduction in any medium or format, as long as you give appropriate credit to the original author(s) and the source, provide a link to the Creative Commons license, and indicate if changes were made. The images or other third party material in this article are included in the article's Creative Commons license, unless indicated otherwise in a credit line to the material. If material is not included in the article's Creative Commons license and your intended use is not permitted by statutory regulation or exceeds the permitted use, you will need to obtain permission directly from the copyright holder. To view a copy of this license, visit <http://creativecommons.org/licenses/by/4.0/>.

the basal forebrain (BF) using a novel GPCR-activation-based (GRAB) sensor for adenosine indicates that neurons represent an essential source of extracellular adenosine^{16,17}, implicating that astrocyte-derived adenosine may constitute only a minor part of the extracellular adenosine. This also suggests that astrocyte-derived adenosine may not be critically involved in regulating sleep–wake behavior.

In the current study, we directly tested the involvement of adenosine signaling in sleep–wake regulation by astrocyte activity in two brain regions that are important for sleep–wake control. We examined the relationship between astrocyte Ca^{2+} transients and the dynamics of extracellular adenosine levels using fiber photometry recording and a newly developed adenosine sensor, and investigated the contributions of ATP hydrolysis-derived adenosine to the levels of extracellular adenosine and to the astrocyte Ca^{2+} elevation-induced sleep–wake modulation using transgenic mice lacking a critical enzyme that mediates ATP-adenosine conversion in the extracellular space. In addition, we examined the role of astrocyte activity in increasing extracellular adenosine levels and the control of the sleep–wake cycle, by directly suppressing the Ca^{2+} transients in BF astrocytes via conditional knockout of the receptors that are critical for mediating astrocyte Ca^{2+} activity. Our results strongly suggested that astrocytes in multiple brain regions can regulate the sleep–wake cycle independent of adenosine signaling pathways.

Results

Astrocyte-specific gene expression in the BF

Much controversy in the study of astrocyte function has arisen due to the non-specific leaky expressions of target genes into neurons, and the specificity of various mouse lines and virus-mediated methods differ in different brain regions¹⁴. Thus, we first tested several commonly used methods in order to achieve astrocyte-specific gene expression for recording and manipulating astrocyte activity in the BF. The BF was chosen because it is a well-documented brain region that plays a critical role in sleep–wake regulation^{16,18,19}, and in which adenosine signaling is known to be important^{16,20–22}. We found that the GFAP-Cre¹², hGFAP-CreER²³, and Aldh1l1-Cre²⁴ mouse lines, that were reported to produce astrocyte-specific gene expression in many other brain regions^{23–34}, all labeled cells with apparent neuron-like morphology in the BF (Supplementary Fig. S1), suggesting non-specific leaky expression in neurons. In contrast, a virus-mediated strategy (AAV5 + GfaABC₁D promoter)^{35–39} constantly produced highly specific gene expression in astrocytes in the BF (Fig. 1). Immunohistochemical staining showed highly specific expression of various vectors that were used in the current study, with 93.5%–100% of the target

gene overlapping with cells expressing the astrocyte marker S100 β ^{35,36,40} (Fig. 1).

Note that due to the notable heterogeneity of astrocytes in different brain regions, our finding that multiple approaches cause leaky expression of the transgene in neurons in the BF does not discredit previous studies using these approaches in other brain regions, as long as the specificity of transgene expression has been rigorously verified.

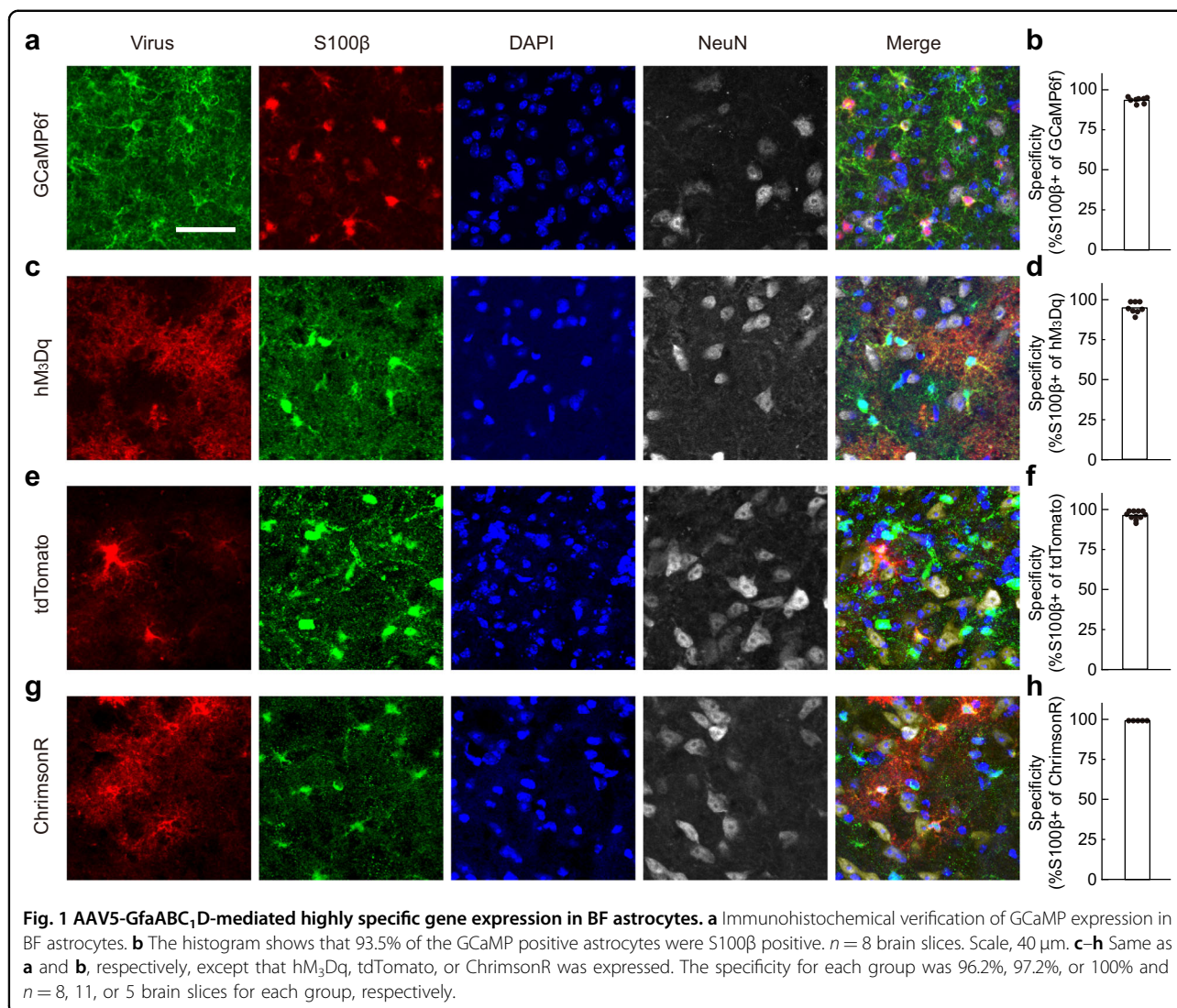
Brain state-dependent Ca^{2+} activity in BF astrocytes

Astrocyte activation is reflected by an elevation of intracellular Ca^{2+} ^{41,42}. We thus first examined the dynamics of astrocyte Ca^{2+} transients during the sleep–wake cycle in the BF using in vivo fiber photometry recording of genetically encoded Ca^{2+} indicator, GCaMP6f⁴³, while simultaneously recording EEG and EMG in free-moving mice (Fig. 2a). The GCaMP6f was expressed in astrocytes of the mouse BF via local injection of a viral vector expressing GfaABC₁D-GCaMP6f^{37,44} (Supplementary Fig. S2).

The population Ca^{2+} activity in astrocytes showed dynamic changes in a brain state-dependent manner (Fig. 2b, c), which was absent in a control condition in which the GCaMP was illuminated with isobestic excitation light (405 nm) (Fig. 2b, d)^{45,46}. The astrocyte Ca^{2+} activity was high during both wakefulness and rapid-eye-movement (REM) sleep and low during non-REM (NREM) sleep (Fig. 2c; Wake vs NREM: $**P = 0.0039$, Wilcoxon signed-rank test; REM vs NREM: $***P < 0.001$, Paired *t*-test), showing rapid dynamics during brain state transitions (Fig. 2f). There was also a high correlation between astrocyte Ca^{2+} activity and locomotion of the mice (Fig. 2e, $**P = 0.0039$, Wilcoxon signed-rank test)^{47–52}. This vigilant state-dependent, rapid dynamic change of astrocyte Ca^{2+} activity during the sleep–wake cycle is highly similar to previously reported neuronal activity in BF^{16,19}, suggesting that astrocyte and neuronal activity dynamics are closely correlated. Such dynamic change of astrocyte Ca^{2+} activity in the BF is also largely consistent with previous measurements in the cortex^{51–53}, hippocampus⁵⁴, and several subcortical regions⁵⁴.

Sleep–wake modulation by astrocyte Ca^{2+} activity in the BF

We next examined how the Ca^{2+} elevation in BF astrocytes contributes to sleep–wake regulation by elevating astrocyte Ca^{2+} with a chemogenetic method⁵⁵. We first injected a viral vector that specifically expressed GfaABC₁D-hM₃Dq (a designer receptor exclusively activated by designer drugs, DREADDs)^{55,56} in BF astrocytes (Fig. 3a–n and Supplementary Fig. S3), and 2 weeks later, we injected the hM₃Dq ligand, clozapine-*N*-oxide (CNO), intraperitoneally (i.p.) in the mice to evoke Ca^{2+} transients in the astrocytes. Mice injected with virus expressing GfaABC₁D-tdTomato were used as the control



group. We confirmed that CNO application produced a large elevation of both tonic and phasic Ca²⁺ activity in astrocytes using both brain slices (Fig. 3a–c) and live mouse preparations (Fig. 3d–f).

To quantify sleep–wake regulation by chemogenetically-induced astrocyte Ca²⁺ activation, we calculated statistical significance using the two-way repeated measures ANOVA with group (hM₃Dq vs tdTomato) and treatment (CNO vs saline) as factors, followed by Tukey's post hoc multiple comparison test when significant main effects were found ($\alpha = 0.05$). The statistical approach was chosen because CNO has been shown to be metabolized into clozapine^{57,58}, which activates multiple monoamine receptors implicated in sleep–wake regulation; two-way ANOVA can unmask the nonspecific effects of CNO and reveal the effects of astrocyte Ca²⁺ activation. In our experiments, we consistently observed modest increases in NREM sleep following injection of low doses of CNO (0.5–1 mg/kg) in

tdTomato-expressing mice. Therefore, in all the following behavioral experiments involving CNO treatment, we mainly report the statistical results from Tukey's post hoc test between the hM₃Dq-CNO group and tdTomato-CNO, unless otherwise stated.

The chemogenetically-induced astrocyte Ca²⁺ elevation significantly changed the sleep–wake behavior of the mice (Fig. 3g–j and Supplementary Fig. S3c). The most prominent effect was a decrease in the total time of REM sleep in the hM₃Dq-CNO group (Fig. 3h; decreased by 28%; ****P* < 0.001), without apparent changes in the duration of wakefulness or NREM sleep (Fig. 3h; Wake, *P* = 0.084; NREM, *P* = 0.57; two-way repeated measures ANOVA). The reduction in REM sleep was not observed in mice injected with the control virus expressing GfaABC₁D-tdTomato (Fig. 3h; *P* = 1.0). Further analysis suggested that the reduction in REM sleep was mainly due to the reduction of REM bouts (Fig. 3i; **P* = 0.033), which

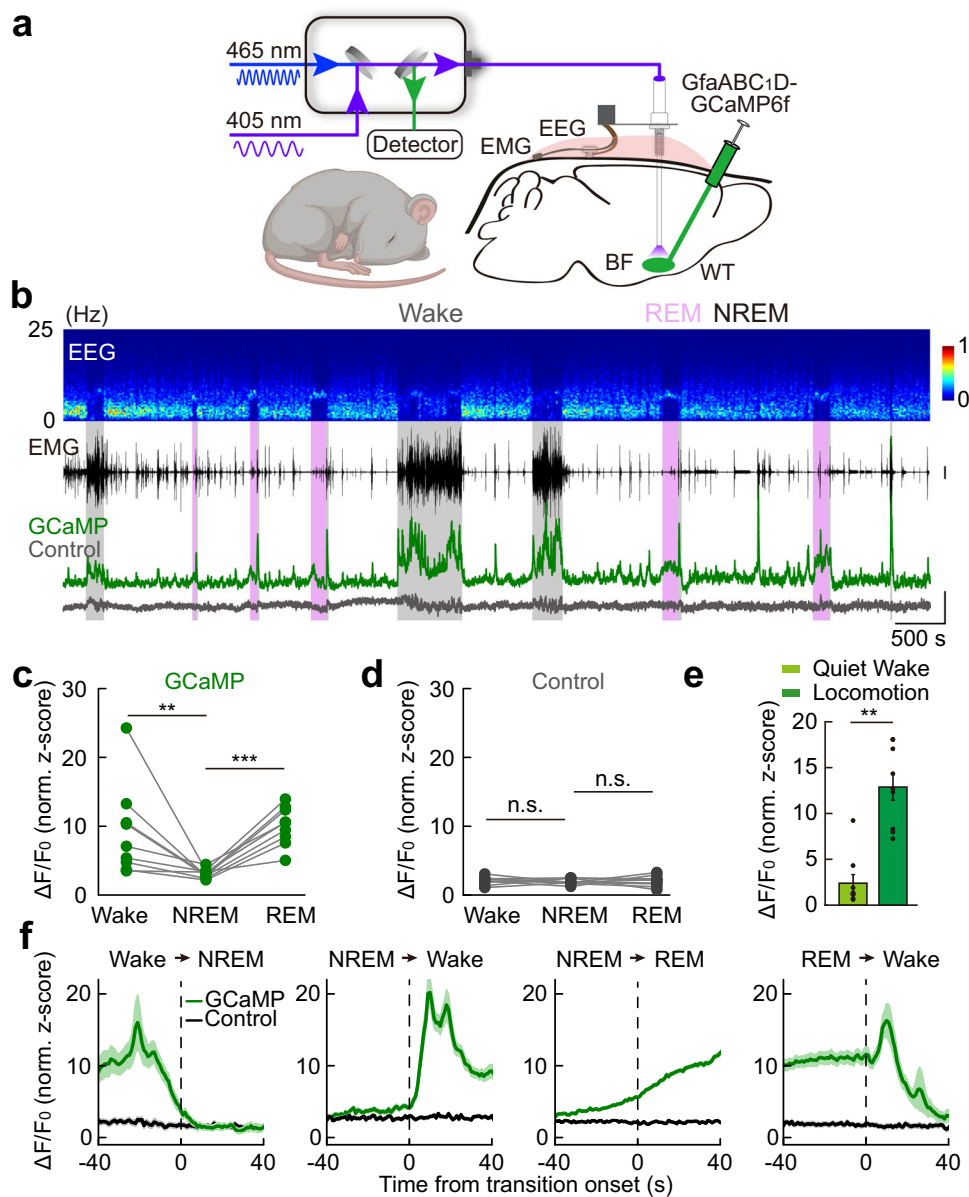


Fig. 2 Brain state-dependent astrocyte Ca^{2+} activity in the BF during the sleep-wake cycle. **a** Schematic diagram depicting fiber photometry recording of astrocyte Ca^{2+} transients in the BF during the sleep-wake cycle. **b** Top to bottom: EEG power spectrogram; EMG (scale, 1 mV); photometry signals of GCaMP (green) and isosbestic excitation (gray) (scale, 1 z-score). The brain states are color-coded; the same color coding is used in all the following figures. **c** GCaMP fluorescence in different brain states. Each line represents data from one recording. $n = 9$ sessions from 4 mice; Wake vs NREM: $**P = 0.0039$ (Wilcoxon signed-rank test); REM vs NREM: $***P < 0.001$ (Paired t -test). In this and all subsequent figures, summary data are expressed as the means \pm SEM. **d** Fluorescence of the isosbestic excitation of GCaMP in different brain states. $n = 9$ sessions from 4 mice. n.s., not significant; Wake vs NREM: $P = 0.74$; REM vs NREM: $P = 0.85$; Paired t -test. **e** Astrocyte Ca^{2+} signal during quiet wakefulness and locomotion. $n = 9$ recording sections from 3 mice for both groups. $**P = 0.0039$ (Wilcoxon signed-rank test). **f** GCaMP and control signal during brain state transitions. The vertical dashed lines represent the transition time. $n = 39, 134, 262,$ and 43 events from 4 mice for each panel, respectively.

was likely caused by increased fragmentation of the NREM sleep, as shown by the increased bout number of NREM and wakefulness and decreased bout duration of NREM after CNO injection (Fig. 3i, j; bout number: NREM, $**P = 0.0028$; Wake, $**P = 0.0026$; bout duration: NREM, $*P = 0.029$; Wake, $P = 0.22$).

The EEG spectrum during sleep was also changed by chemogenetic activation of the BF astrocytes (Fig. 3k–n). There were significant decrease of NREM delta power (0.5–4 Hz) (Fig. 3l; $*P = 0.039$) and increase of theta power (4–8 Hz) during both NREM and REM sleep (Fig. 3l, n; NREM, $*P = 0.014$; REM, $**P = 0.0041$). These

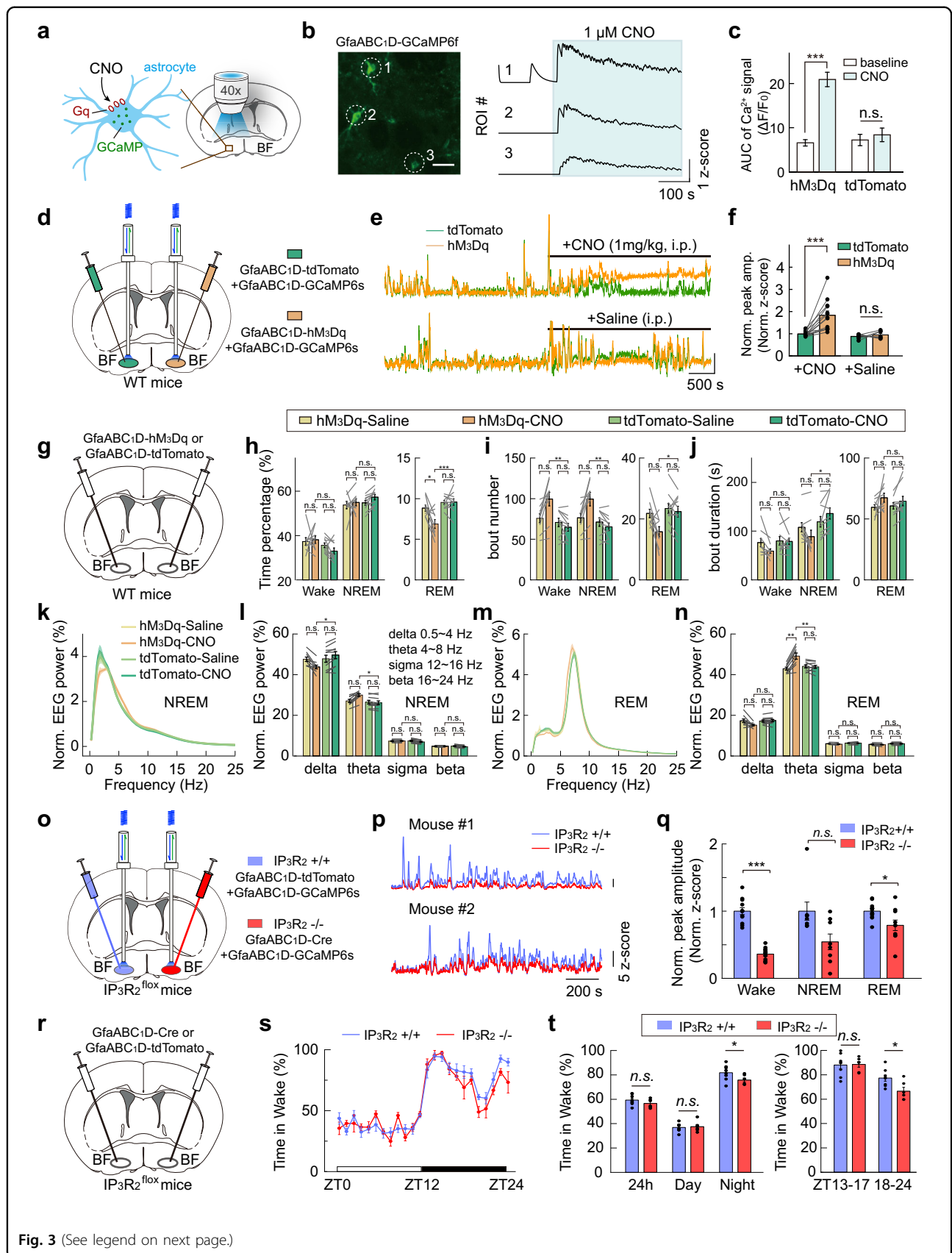


Fig. 3 (See legend on next page.)

(see figure on previous page)

Fig. 3 Sleep–wake modulation by astrocyte Ca^{2+} activity in the BF. **a** Schematic diagram depicting Ca^{2+} imaging from hM₃Dq-expressing astrocytes in brain slices. **b** Left, confocal image showing GCaMP-expressing astrocyte in a brain slice (scale, 50 μm); right, Ca^{2+} signals of the individual region of interest (ROI). **c** Quantification of CNO-evoked Ca^{2+} signals. AUC, area under the curve. AUC measures the area of Ca^{2+} signals during baseline (the 2-min period prior to CNO infusion) and after bath application of CNO (2 min). hM₃Dq group: $n = 99$ ROIs; $***P < 0.001$. tdTomato group: $n = 51$ ROIs; $P = 0.093$. (Paired t -test). **d–f** Chemogenetic activation of BF astrocytes in live mice. **d** Schematic diagram depicting fiber photometry recording of chemogenetic activation-induced astrocyte Ca^{2+} signal. AAVs expressing GfaABC₁D-tdTomato and GfaABC₁D-GCaMP6s were injected into the BF of one hemisphere, and AAVs expressing GfaABC₁D-hM₃Dq and GfaABC₁D-GCaMP6s were injected into the contralateral BF. **e** Example traces showing astrocyte Ca^{2+} signal from the BF expressing tdTomato (green) or hM₃Dq (yellow), respectively. Free-behaving mice were injected with CNO (1 mg/kg, i.p.) or saline (i.p.). Scale, 2 normalized z-score. **f** Quantitative comparison of astrocyte Ca^{2+} signal from the BF expressing tdTomato (green) or hM₃Dq (yellow) in response to CNO or saline injections. The mean ratio between the size of astrocyte Ca^{2+} events from the hM₃Dq- and tdTomato-expressing BF was calculated before and after CNO or saline injections. CNO injection significantly increased the size of GCaMP events in hM₃Dq-expressing BF (186% increase, $***P < 0.001$, Paired t -test), whereas saline injection had no detectable effect ($P = 0.43$, Paired t -test). CNO injections, $n = 13$ sessions from 4 mice; Saline injections, $n = 7$ sessions from 4 mice. **g** Schematic diagram depicting chemogenetic activation of astrocytes in the BF in wide-type (WT) mice. **h–n** Chemogenetic activation of BF astrocytes in WT mice significantly changed sleep–wake behavior (within the 4 h after CNO injection). hM₃Dq group, $n = 9$ mice; tdTomato group, $n = 10$ mice. The statistical method was two-way repeated measures ANOVA, followed by Tukey's post hoc multiple comparison test. Time percentage (**h**), bout number (**i**), and bout duration (**j**) of the three brain states after CNO or saline injections. In **h**, hM₃Dq-CNO vs tdTomato-CNO: Wake, $P = 0.084$; NREM, $P = 0.57$; REM, $***P < 0.001$. hM₃Dq-Saline vs hM₃Dq-CNO: Wake, $P = 0.98$; NREM, $P = 0.92$; REM, $*P = 0.012$. tdTomato-Saline vs tdTomato-CNO: Wake, $P = 0.54$; NREM, $P = 0.49$; REM, $P = 1.0$. In **i**, hM₃Dq-CNO vs tdTomato-CNO: Wake, $**P = 0.0026$; NREM, $**P = 0.0028$; REM, $*P = 0.033$. hM₃Dq-Saline vs hM₃Dq-CNO: Wake, $P = 0.051$; NREM, $P = 0.054$; REM, $P = 0.065$. tdTomato-Saline vs tdTomato-CNO: Wake, $P = 0.87$; NREM, $P = 0.88$; REM, $P = 0.96$. In **j**, hM₃Dq-CNO vs tdTomato-CNO: Wake, $P = 0.22$; NREM, $*P = 0.029$; REM, $P = 0.91$. hM₃Dq-Saline vs hM₃Dq-CNO: Wake, $P = 0.34$; NREM, $P = 0.62$; REM, $P = 0.31$. tdTomato-Saline vs tdTomato-CNO: Wake, $P = 1.0$; NREM, $P = 0.67$; REM, $P = 0.79$. **k** Normalized NREM EEG power after the injection of CNO or saline in hM₃Dq- or tdTomato-expressing mice. **l** Quantification of NREM EEG power in delta, theta, sigma, and beta bands. hM₃Dq-CNO vs tdTomato-CNO: delta, $*P = 0.039$; theta, $*P = 0.014$; sigma, $P = 0.54$; beta, $P = 0.60$. hM₃Dq-Saline vs hM₃Dq-CNO: delta, $P = 0.27$; theta, $P = 0.083$; sigma, $P = 1.0$; beta, $P = 1.0$. tdTomato-Saline vs tdTomato-CNO: delta, $P = 0.79$; theta, $P = 0.99$; sigma, $P = 0.46$; beta, $P = 0.42$. **m, n** Same as **k, l**, except that REM EEG was analyzed. In **n**, hM₃Dq-CNO vs tdTomato-CNO: delta, $P = 0.065$; theta, $**P = 0.0041$; sigma, $P = 0.16$; beta, $P = 0.17$. hM₃Dq-Saline vs hM₃Dq-CNO: delta, $P = 0.091$; theta, $**P = 0.0012$; sigma, $P = 0.71$; beta, $P = 0.86$. tdTomato-Saline vs tdTomato-CNO: delta, $P = 0.99$; theta, $P = 1.0$; sigma, $P = 1.0$; beta, $P = 1.0$. **o–q** IP₃R₂ knockout (KO) reduced astrocyte Ca^{2+} activity during both wakefulness and REM sleep. **o** Schematic diagram depicting fiber photometry recording of astrocyte Ca^{2+} signal in the BF to examine the effect of IP₃R₂-KO. **p** Example astrocyte Ca^{2+} signal from the BF expressing Cre (red, IP₃R₂^{-/-}) or control virus (light blue, IP₃R₂^{+/+}), respectively. Scale bar = 200 s and 5 z-score. **q** Quantitative comparison of astrocyte Ca^{2+} signal from the BF expressing Cre (red, IP₃R₂^{-/-}) or control virus (light blue, IP₃R₂^{+/+}) during different brain states. Wake, reduced by 64%, $***P < 0.001$, Paired t -test; NREM, $P = 0.078$, Wilcoxon signed-rank test; REM, reduced by 21%, $*P = 0.021$, Paired t -test; $n = 12$ recordings from 4 mice (3 recordings per mouse). **r–t** IP₃R₂-KO in BF astrocytes reduced wakefulness in the late phase of the night. **r** Schematic diagram of suppressing astrocyte Ca^{2+} elevation in the BF using the IP₃R₂^{flox} mice. **s** Circadian variation of wakefulness in the two groups. $n = 6$ and 8 mice for Cre group and tdTomato group, respectively. **t** Percentage of wakefulness in the entire 24 h, during the day, during the night, and the early (ZT13–17) or late phase (ZT18–24) of the night. 24 h, $P = 0.21$; Day, $P = 0.79$; Night, $*P = 0.049$; ZT13–17, $P = 0.90$; ZT18–24, $*P = 0.022$; Student's t -test.

results suggest that astrocyte activation in the BF can modulate the sleep–wake cycle by decreasing the consolidation and depth of NREM sleep, as indicated by increased NREM fragmentation and decreased NREM delta power, respectively.

To further address the physiological role of the BF astrocytes in sleep–wake regulation, we performed a loss-of-function experiment (Fig. 3o–t and Supplementary Fig. S4) by selectively suppressing Ca^{2+} elevation in BF astrocytes using the IP₃R₂^{flox} mice⁵⁹, which provides genetic access to the receptor, inositol 1,4,5-trisphosphate (IP₃) receptor type 2 (IP₃R₂), that mediates a significant part of Ca^{2+} increase in astrocyte⁶⁰. Injection of GfaABC₁D-Cre into the BF of the IP₃R₂^{flox} mice suppressed astrocyte Ca^{2+} transient during the sleep–wake cycle, with a marked decrease in wakefulness (64% reduction, $***P < 0.001$, Paired t -test), moderate decrease in REM sleep (21% reduction, $*P = 0.021$, Paired t -test), and no significant change in NREM sleep ($P = 0.078$, Wilcoxon signed-rank test) (Fig. 3p, q). Bilateral injection

of GfaABC₁D-Cre in the BF of the IP₃R₂^{flox} mice (Fig. 3r and Supplementary Fig. S4a, b) caused a significant decrease in wakefulness, especially in the late phase of the night (Fig. 3s, t; ZT18–24 $*P = 0.022$, Student's t -test), without affecting the sleep–wake states during other time of the day (Fig. 3s, t and Supplementary Fig. S4c–f). These results indicated that BF astrocytes play a role in supporting wakefulness under physiological conditions.

Astrocyte Ca^{2+} activity in the BF is highly correlated with the extracellular levels of ATP and adenosine

We next tested the involvement of adenosine signaling in the astrocyte Ca^{2+} elevation-induced sleep–wake modulation. To measure extracellular adenosine levels, we used a genetically encoded sensor, GRAB_{Ado}¹⁶. GRAB_{Ado} is an engineered chimera protein that is made by replacing the 3rd intracellular loop of the adenosine A_{2A} receptor with a conformation-sensitive circularly permuted enhanced GFP (cpEGFP), so that the amount of extracellular adenosine is indicated by the cpGFP

fluorescence intensity. GRAB_{Ado} inherits the molecule selectivity of the adenosine A_{2A} receptor and has rapid response kinetics, with a rising time constant of 70 ms and high sensitivity of 60 nM as measured by the median effective concentration (EC₅₀). Its fluorescence intensity correlates with adenosine level within a broad range (~1 nM–10 μM), which covers the extracellular adenosine level under physiological conditions (estimated between ten and a few hundred nM)^{61,62}. The measurement of extracellular ATP level was achieved by using the ATP GRAB sensor (GRAB_{ATP})⁶³.

Whether the astrocyte Ca²⁺ transients correlate with the change in extracellular adenosine was examined by fiber photometry recording with the “bilateral dual probes” method¹⁶ that simultaneously monitored astrocyte Ca²⁺ (with GCaMP6f) and extracellular adenosine (with GRAB_{Ado}) in the BF of two different hemispheres (Fig. 4a and Supplementary Fig. S5a, b). AAVs expressing GfaABC_{1D}-GCaMP6f were injected into one hemisphere of the BF, and AAVs expressing hSyn-GRAB_{Ado} were injected into the contralateral hemisphere of the BF. This dual-probe method allows the simultaneous recording of fluorescence signals with an overlapping emission wavelength in the same brain region. The GRAB_{Ado} sensor has widely distributed expression, so it can report adenosine release in both soma and processes of neurons or astrocytes^{16,64}. We found that, during the sleep–wake cycle, the spontaneous increase of astrocyte Ca²⁺ activity and extracellular adenosine had a similar time course (Fig. 4b), with the magnitude of the two signals highly correlated (Fig. 4c; Pearson’s $r = 0.69$, *** $P < 0.001$). Such correlation was not observed in the control analysis, in which the GCaMP signals were temporally shuffled in a random manner (Fig. 4d; Pearson’s $r = 0.07$)¹⁶. More importantly, changes in astrocyte Ca²⁺ activity preceded that of the adenosine signal by approximately 23 s (Fig. 4e), suggesting that astrocyte activity may regulate the amount of extracellular adenosine^{8,11}.

Astrocyte-derived adenosine is known to be produced by hydrolysis of astrocyte-released ATP in the extracellular space^{11,65,66}. We thus next measured the dynamics of astrocyte Ca²⁺ activity and extracellular ATP level simultaneously in the BF, using the same “bilateral dual probes” method (Fig. 4f and Supplementary Fig. S5c, d). We found that the astrocyte Ca²⁺ and ATP signals were highly correlated in the time course and the magnitude (Fig. 4g–j). Interestingly, the change in ATP signal immediately followed the change in astrocyte Ca²⁺ signal with a delay of about 1 s (Fig. 4j). This result is consistent with previous findings that astrocytes are an important source of extracellular ATP¹⁵.

The measurements of astrocyte Ca²⁺ activity and extracellular adenosine and ATP levels predict that changes in ATP levels may precede changes in adenosine

levels by approximately 22 s. Consistent with this prediction, our simultaneous recording of extracellular adenosine and ATP levels in the BF using the “bilateral dual probes” method revealed an actual difference of approximately 22 s (Fig. 4k–o and Supplementary Fig. S5e, f), furthering supporting that ATP release may underlie the increase of extracellular adenosine¹⁵.

Optogenetically evoked astrocyte Ca²⁺ elevation causes no detectable adenosine increase

To directly examine the causal relationship between astrocyte Ca²⁺ elevation and extracellular adenosine increase in the BF, we evoked astrocyte Ca²⁺ activity optogenetically and used fiber photometry to measure the adenosine level by local injection of AAVs expressing GRAB_{Ado} and astrocyte-specific red-shifted channelrhodopsin, GfaABC_{1D}-ChrimsonR⁶⁷ (Supplementary Fig. S6). Although laser light (638 nm laser, 10 ms/pulse, 10 Hz for 10 s) could reliably induce a significant increase in astrocyte Ca²⁺ elevation (Supplementary Fig. S7; ** $P = 0.0011$, Student’s t -test), we found no detectable increase in extracellular adenosine after laser application (Supplementary Fig. S6d; $P = 0.39$, Student’s t -test), in contrast to the previously reported prominent adenosine increase by optogenetic neuronal activation in the same brain region¹⁶. Thus, astrocyte Ca²⁺ elevation does not always induce an increase in extracellular adenosine. This result raises the possibility that astrocyte Ca²⁺ activity may not be the major cause of the observed extracellular adenosine increase in the BF during the sleep–wake cycle.

The use of optogenetic methods provided a time-locked stimulation-analysis window, thus ensuring highly sensitive measurements of the causal relationship between astrocyte Ca²⁺ elevation and extracellular adenosine increase. However, it is also possible that optogenetic stimulation-induced astrocyte Ca²⁺ differs from that occurs physiologically during the sleep–wake cycle, as reported previously^{68,69}. We thus performed additional experiments to further examine the involvement of astrocyte-derived adenosine in the modulation of the sleep–wake cycle.

Adenosine level dynamics and astrocyte Ca²⁺ elevation-induced sleep–wake modulation are not affected in the CD73-KO mice

Astrocytes are thought to increase extracellular adenosine by releasing ATP, which is then hydrolyzed to adenosine by a series of ecto-enzymes^{70,71}, including the key enzyme CD73 (encoded by *Nt5e*) that converts AMP to adenosine^{17,72}. If astrocyte-derived ATP represents a significant contributor to extracellular adenosine during the sleep–wake cycle, we would expect that blocking CD73 activity would substantially reduce the amount of extracellular adenosine and its correlation with extracellular

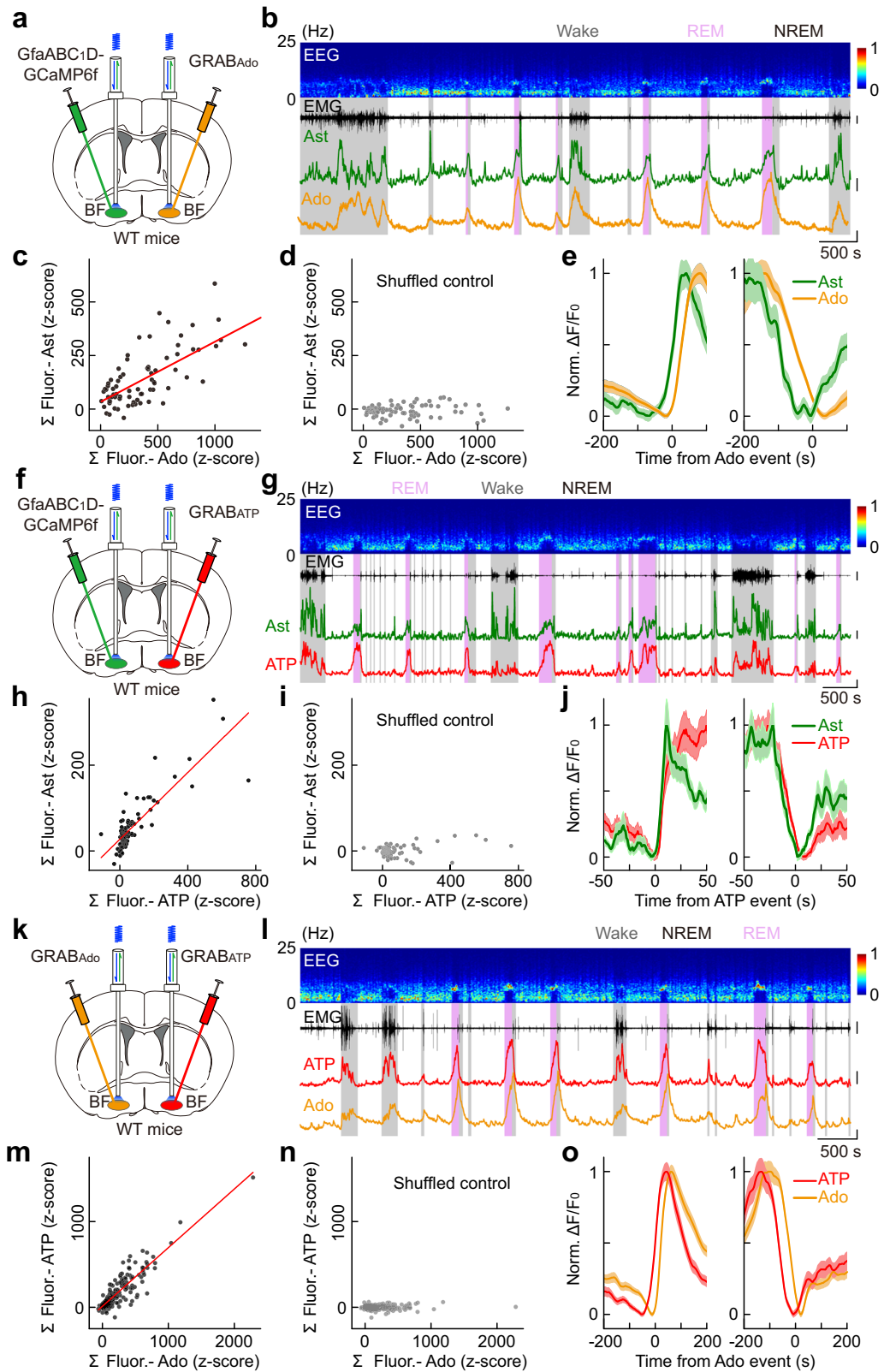


Fig. 4 (See legend on next page.)

(see figure on previous page)

Fig. 4 Astrocyte Ca^{2+} elevation in the BF is highly correlated with the dynamics of extracellular adenosine and ATP levels. **a** Schematic diagram depicting fiber photometry recording of extracellular adenosine level and population Ca^{2+} signal of astrocytes in the BF during the sleep–wake cycle. **b** Top to bottom, EEG power spectrogram, EMG (scale, 0.5 mV), GCaMP fluorescence (scale, 1 z-score), and GRAB_{Ado} fluorescence (scale, 1 z-score). **c** Correlation between the size of GCaMP and GRAB_{Ado} events. The red line represents a linear fit. $n = 76$ events from 7 recordings in 4 mice. Pearson's $r = 0.69$, $***P < 0.001$. **d** Same as in **c** after the GCaMP signal was randomly shuffled. Pearson's $r = 0.07$. **e** Time course of the GCaMP and GRAB_{Ado} signal aligned to the onset (left) or offset (right) of the GRAB_{Ado} events. **f–j** Same as **a–e**, respectively, except that population Ca^{2+} signal of astrocytes and extracellular ATP were measured. Scale bar in **g**: EMG, 2 mV; GCaMP, 1 z-score; GRAB_{ATP}, 1 z-score. In **h**: $n = 88$ events from 8 recordings in 4 mice. Pearson's $r = 0.84$, $***P < 0.001$. In **i**: Pearson's $r = 0.32$. **k–o** Same as **a–e**, respectively, except that extracellular adenosine and ATP were measured. Scale bar in **l**: EMG, 0.5 mV; GRAB_{Ado}, 1 z-score; GRAB_{ATP}, 1 z-score. In **m**: $n = 199$ events from 15 recordings in 4 mice. Pearson's $r = 0.89$, $***P < 0.001$. In **n**: Pearson's $r = 0.10$.

ATP. However, in the BF of CD73 KO mice^{73,74}, using fiber photometry recording of GRAB_{Ado}, we detected a notable increase in adenosine signal during both wakefulness and REM sleep, with no significant difference from that previously reported in the WT mice¹⁶ (Fig. 5a, b and Supplementary Fig. S8a, b; CD73-KO vs WT: Wake, $P = 0.41$; REM, $P = 0.76$; Wilcoxon rank-sum test; Data for WT mice were reported previously in Fig. 4l of Peng et al.¹⁶). This result indicates that CD73-mediated, ATP hydrolysis-derived adenosine does not contribute significantly to the amount of extracellular adenosine in the BF during the sleep–wake cycle^{17,75,76}.

Further support for this conclusion was provided by our finding that bilateral dual-probe measurements of extracellular adenosine and ATP in the BF of CD73-KO mice during the sleep–wake cycle (Fig. 5c–g and Supplementary Fig. S8c, d) showed that the dynamics of extracellular ATP and adenosine was not significantly different from that of the WT mice, with the two signals remained highly correlated in both the time course and magnitude.

In line with these results, the hM₃Dq-induced astrocyte Ca^{2+} elevation in the BF caused comparable modulation to the sleep–wake behavior in CD73-KO mice as that in WT mice (Fig. 5h–k and Supplementary Fig. S9), with a significant decrease in the total time of REM sleep (Fig. 5i; reduced by 26%, $***P < 0.001$), REM bout number (Fig. 5j; $*P = 0.017$), and fragmented NREM sleep as indicated by the increased bout number and decreased bout duration of both NREM and wakefulness (Fig. 5j, k; bout number: NREM, $***P < 0.001$; Wake, $***P < 0.001$; bout duration: NREM, $***P < 0.001$; Wake, $**P = 0.0028$). Moreover, the EEG spectrum also exhibited similar changes as that in WT mice (Fig. 5l–o) (EEG delta power: NREM, $P = 0.063$; REM, $P = 0.53$; EEG theta power: NREM, $P = 0.18$; REM, $***P < 0.001$).

Suppressing Ca^{2+} elevation in BF astrocytes decreases the extracellular levels of ATP but not adenosine

Because an alternative explanation for our above observations could be that extracellular ATP–adenosine conversion in the BF is mediated by other ectoenzymes

rather than CD73, we directly tested the contribution of BF astrocytes to the elevation of extracellular adenosine by suppressing the astrocyte Ca^{2+} elevation using the IP₃R₂^{fl_{ox}} mice⁵⁹. We selectively deleted the IP₃R₂ receptors from BF astrocytes by injecting a viral vector expressing GfaABC₁D-Cre and compared the extracellular level of ATP and adenosine with that in the contralateral BF (injected with a control vector expressing GfaABC₁D-tdTomato) in the same mouse (Fig. 6 and Supplementary Fig. S10). This IP₃R₂-KO-induced suppression of astrocyte Ca^{2+} elevation caused a significant decrease of the extracellular level of ATP (Fig. 6b, c) (Wake, $**P = 0.0098$, Wilcoxon signed-rank test; NREM, $**P = 0.0033$, Paired *t*-test; REM, $*P = 0.042$, Paired *t*-test), consistent with the notion that astrocytes are an important source of extracellular ATP^{65,77}; however, we observed no detectable change in the extracellular level of adenosine (Fig. 6e, f) (Wake, $P = 0.48$, Paired *t*-test; NREM, $P = 0.27$, Wilcoxon signed-rank test; REM, $P = 0.34$, Paired *t*-test). This uncorrelated change in the amount of extracellular ATP and adenosine further supported the above notion that ATP hydrolysis-derived adenosine does not contribute significantly to the amount of extracellular adenosine in the BF during the sleep–wake cycle. These results strongly suggested that astrocyte activity is not a significant factor in increasing extracellular adenosine in the BF during the sleep–wake cycle, further implying that astrocyte Ca^{2+} elevation may modulate the sleep–wake behavior through adenosine-independent pathways.

Ca^{2+} elevation in BF astrocyte modulates local neural network

Astrocyte Ca^{2+} elevation can modulate the activity of neuronal networks^{42,78–80}, which may underlie the astrocyte Ca^{2+} elevation-induced sleep–wake modulation in the BF. We thus examined the changes in the synaptic activity in BF brain slices using patch-clamp recording following acute hM₃Dq-induced astrocyte Ca^{2+} elevation in the BF in vivo³⁶ (Fig. 7a–c and Supplementary Fig. S11). We found that, compared with the control group (brain

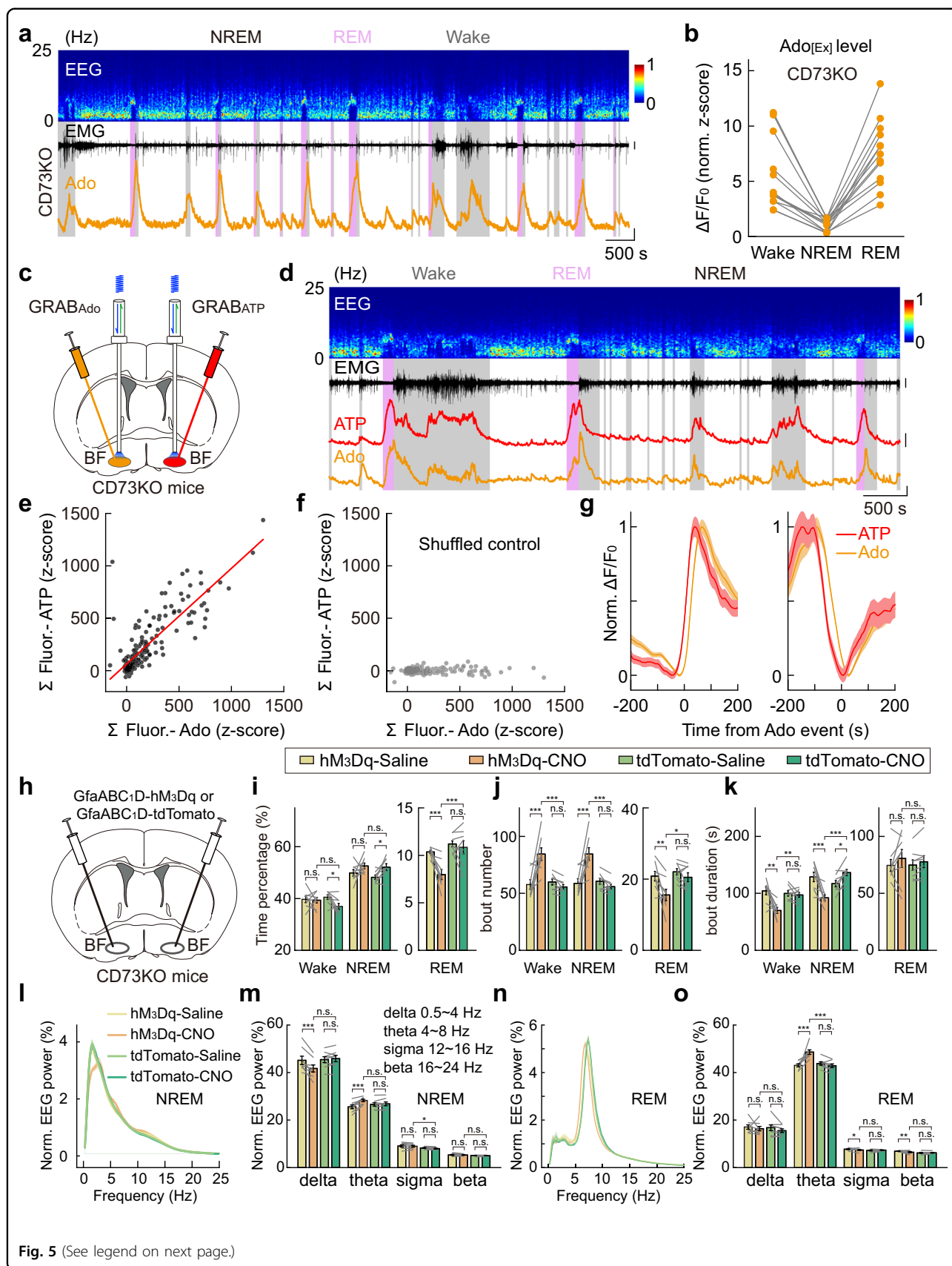


Fig. 5 (See legend on next page.)

(see figure on previous page)

Fig. 5 CD73-KO mice show normal extracellular adenosine dynamics and astrocyte Ca^{2+} elevation-induced modulation to the sleep-wake cycle. **a** Recording of adenosine signal in the BF during the sleep-wake cycle in CD73-KO mice. Top to bottom: EEG power spectrogram, EMG (scale, 1 mV), and GRAB_{Ado} fluorescence (scale, 1 z-score). **b** GRAB_{Ado} signal in CD73-KO mice in different brain states. Each line represents data from one recording. $n = 13$ sessions from 6 mice. CD73KO vs WT (reported previously in Fig. 4I in Peng et al.): Wake, $P = 0.41$; REM, $P = 0.76$; Wilcoxon rank-sum test. **c-g** Same as Fig. 4k-o, respectively, except that experiments were performed using CD73-KO mice. Scale bar in **d**: EMG, 1 mV; GRAB_{Ado}, 1 z-score; GRAB_{ATP}, 1 z-score. In **e**: $n = 187$ events from 14 recordings in 4 mice. Pearson's $r = 0.83$, $***P < 0.001$. In **f**: Pearson's $r = 0.07$. **h-o** Same as Fig. 3g-n, respectively, except that experiments were performed using CD73-KO mice. hM₃Dq group, $n = 8$ mice; tdTomato group, $n = 8$ mice. The statistical method was two-way repeated measures ANOVA, followed by Tukey's post hoc multiple comparison test. In **i**, hM₃Dq-CNO vs tdTomato-CNO: Wake, $P = 0.14$; NREM, $P = 0.78$; REM, $***P < 0.001$. hM₃Dq-Saline vs hM₃Dq-CNO: Wake, $P = 0.85$; NREM, $P = 0.15$; REM, $***P < 0.001$. tdTomato-Saline vs tdTomato-CNO: Wake, $*P = 0.035$; NREM, $*P = 0.042$; REM, $P = 0.51$. In **j**, hM₃Dq-CNO vs tdTomato-CNO: Wake, $***P < 0.001$; NREM, $***P < 0.001$; REM, $*P = 0.017$. hM₃Dq-Saline vs hM₃Dq-CNO: Wake, $***P < 0.001$; NREM, $***P < 0.001$; REM, $**P = 0.0020$. tdTomato-Saline vs tdTomato-CNO: Wake, $P = 0.42$; NREM, $P = 0.38$; REM, $P = 0.30$. In **k**, hM₃Dq-CNO vs tdTomato-CNO: Wake, $**P = 0.0028$; NREM, $***P < 0.001$; REM, $P = 0.73$. hM₃Dq-Saline vs hM₃Dq-CNO: Wake, $**P = 0.0011$; NREM, $**P < 0.001$; REM, $P = 0.21$. tdTomato-Saline vs tdTomato-CNO: Wake, $P = 0.75$; NREM, $*P = 0.022$; REM, $P = 0.52$. In **m**, hM₃Dq-CNO vs tdTomato-CNO: delta, $P = 0.063$; theta, $P = 0.18$; sigma, $*P = 0.045$; beta, $P = 0.18$. hM₃Dq-Saline vs hM₃Dq-CNO: delta, $***P < 0.001$; theta, $***P < 0.001$; sigma, $P = 0.50$; beta, $P = 0.58$. tdTomato-Saline vs tdTomato-CNO: delta, $P = 0.54$; theta, $P = 0.62$; sigma, $P = 0.064$; beta, $P = 0.52$. In **o**, hM₃Dq-CNO vs tdTomato-CNO: delta, $P = 0.53$; theta, $***P < 0.001$; sigma, $P = 0.89$; beta, $P = 0.36$. hM₃Dq-Saline vs hM₃Dq-CNO: delta, $P = 0.47$; theta, $***P < 0.001$; sigma, $*P = 0.023$; beta, $**P = 0.0076$. tdTomato-Saline vs tdTomato-CNO: delta, $P = 0.20$; theta, $P = 0.35$; sigma, $P = 0.28$; beta, $P = 0.69$.

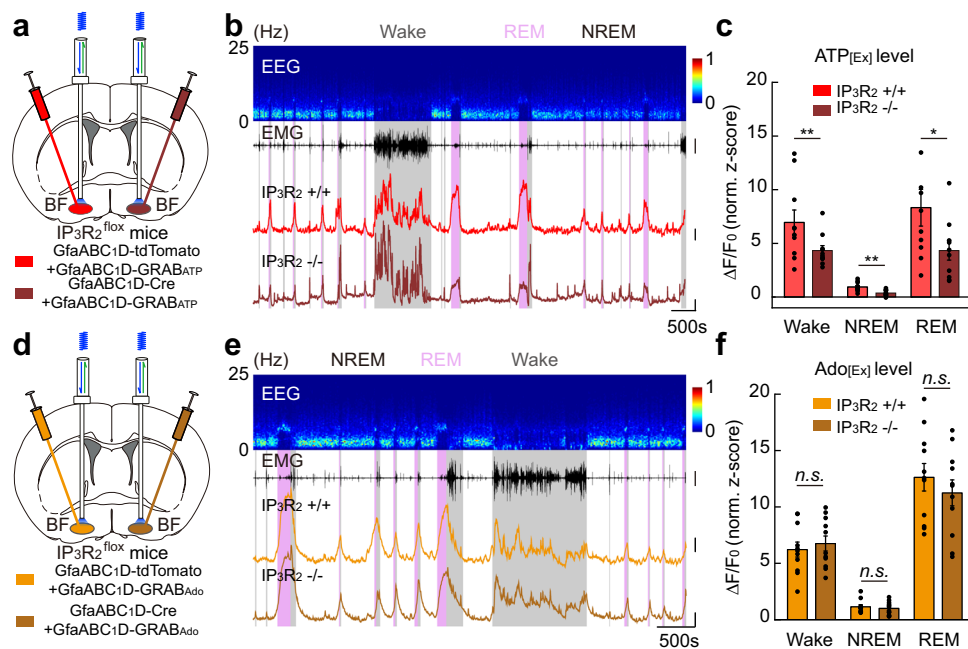


Fig. 6 Suppressing Ca^{2+} elevation in BF astrocytes decreases extracellular level of ATP but not adenosine. **a** Schematic diagram depicting fiber photometry recording of extracellular ATP level in the BF of IP₃R₂^{flox} mice during the sleep-wake cycle. IP₃R₂ receptors from astrocytes were knocked out in one hemisphere of the BF via injection of GfaABC₁D-Cre, and extracellular ATP level from the two hemispheres of the same mouse was compared. **b** Top to bottom, EEG power spectrogram, EMG (scale, 2 mV), and GRAB_{ATP} fluorescence of the two hemispheres, respectively (scale, 1 z-score and 500 s). **c** Quantification of GRAB_{ATP} fluorescence in the two hemispheres. $n = 10$ sessions from 4 mice. Wake, $**P = 0.0098$, Wilcoxon signed-rank test; NREM, $**P = 0.0033$, Paired t -test; REM, $*P = 0.042$, Paired t -test. **d-f** Same as **a-c**, respectively, except that extracellular adenosine level was measured. Scale bar in **e**: EMG, 2 mV; GRAB_{Ado}, 1 z-score. In **f**: $n = 11$ sessions from 4 mice. Wake, $P = 0.48$, Paired t -test; NREM, $P = 0.27$, Wilcoxon signed-rank test; REM, $P = 0.34$, Paired t -test.

slices from mice injected with GfaABC₁D-tdTomato), the hM₃Dq group showed significant increases in both amplitude and frequency of the miniature inhibitory postsynaptic currents (mIPSCs) (amplitude: $**P = 0.005$, Student's t -test; frequency: $***P < 0.001$, Wilcoxon rank-sum test) and the amplitude but not the frequency of

miniature excitatory postsynaptic currents (mEPSCs) (amplitude: $*P = 0.041$, Student's t -test; frequency: $P = 0.48$, Wilcoxon rank-sum test) (Fig. 7b and Supplementary Fig. S11a, c), suggesting that astrocyte Ca^{2+} elevation in the BF increased neuronal transmissions of the local neural network.

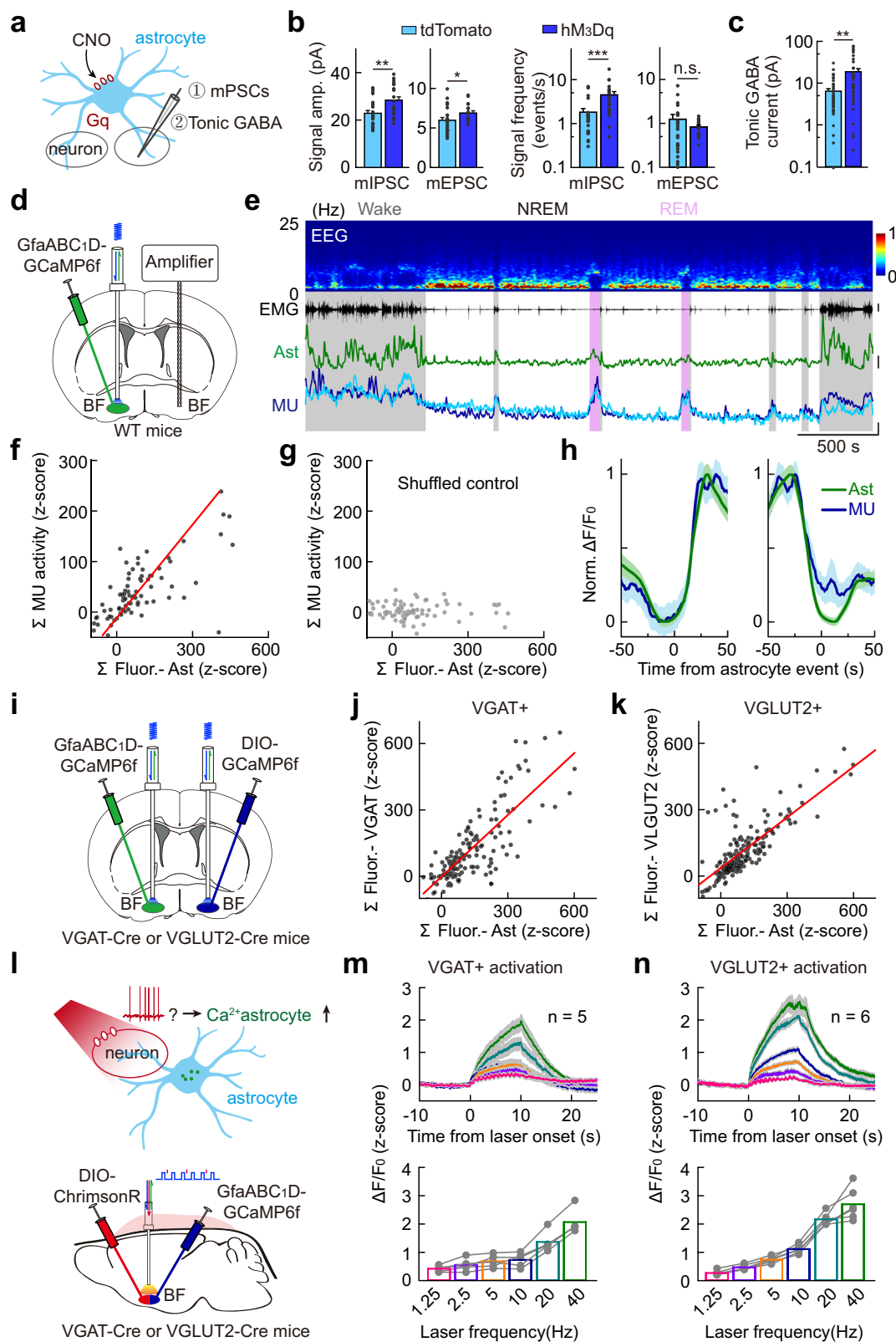


Fig. 7 (See legend on next page.)

(see figure on previous page)

Fig. 7 Astrocyte–neuron interactions in the BF. **a** Schematic diagram depicting patch-clamp recording of BF neurons after activation of hM₃Dq-expressing astrocytes. **b** CNO applications altered miniature synaptic transmissions in hM₃Dq-expressing brain slices. mIPSC: Amplitude, $**P = 0.005$, Student's *t*-test; Frequency, $***P < 0.001$, Wilcoxon rank-sum test; $n = 22$ and 23 cells for hM₃Dq and tdTomato group, respectively. mEPSC: Amplitude, $*P = 0.041$, Student's *t*-test; Frequency, $P = 0.48$, Wilcoxon rank-sum test. $n = 20$ and 24 cells for hM₃Dq and tdTomato group, respectively. **c** CNO applications increased tonic GABA current in hM₃Dq-expressing brain slice. $**P = 0.0011$, Wilcoxon rank-sum test; $n = 38$ and 37 cells for hM₃Dq and tdTomato group, respectively. **d** Schematic diagram depicting simultaneous recording of population Ca²⁺ signal of astrocytes and multi-unit neural activity in the BF during the sleep–wake cycle. **e** Top to bottom, EEG power spectrogram, EMG (scale, 0.1 mV), GCaMP fluorescence (scale, 1 z-score), and multi-unit neural activity (scale, 1 z-score). **f–h** Same as Fig. 4c–e, respectively, except that extracellular Ado and multi-unit neural activity were compared. $n = 80$ events from 9 recordings in 3 mice. In **f**, Pearson's $r = 0.70$, $***P < 0.001$; in **g**, Pearson's $r = -0.01$. **i** Schematic diagram depicting simultaneous recording of population Ca²⁺ signal of astrocytes and VGAT⁺ or VGLUT2⁺ neurons in the BF during the sleep–wake cycle. **j** Correlation between the size of GCaMP events in astrocytes and VGAT⁺ neurons. The red line represents a linear fit. $n = 156$ events from 8 recordings in 3 mice. Pearson's $r = 0.80$, $***P < 0.001$. **k** Same as **j**, except that GCaMP events in astrocytes and VGLUT2⁺ neurons were compared. $n = 139$ events from 9 recordings in 3 mice. Pearson's $r = 0.76$, $***P < 0.001$. **l** Schematic diagram depicting fiber photometry recording of GCaMP signals in astrocytes induced by optogenetic activation of VGAT⁺ or VGLUT2⁺ neurons. **m** Summary of evoked GCaMP signals in astrocytes induced by optogenetic activation of VGAT⁺ neurons using different frequencies (shown in different colors) of laser pulses. $n = 5$ mice. **n** Same as **m**, except that VGLUT2⁺ neurons were activated. $n = 6$ mice.

We next measured the tonic inhibition of BF neurons following hM₃Dq-induced astrocyte Ca²⁺ elevation in the BF in vivo, because astrocytes are known to regulate ambient GABA levels^{36,81–83}. GABA tonic inhibition was measured by bath application of GABA_A receptor antagonist (SR95531, 20 μM) and recording the changes in holding current at -70 mV³⁶ (Supplementary Fig. S11b). Tonic inhibition was significantly larger in mice with hM₃Dq-induced astrocyte Ca²⁺ elevation in the BF, compared with that from the control group (CNO treatment in mice injected with AAVs expressing GfaABC1D-tdTomato) (Fig. 7c; $**P = 0.0011$, Wilcoxon rank-sum test). Together, these results show that astrocyte Ca²⁺ elevation in the BF can cause various modulations to the local neural network, which may then produce the modulation of the sleep–wake cycle.

Our previous work shows that activation of VGLUT2⁺ neurons in the BF causes a large increase in extracellular adenosine levels. Therefore, our data that activation of astrocytes in the BF produced no detectable increase in adenosine level suggested that astrocyte activation cannot cause a large increase in the activity of VGLUT2⁺ neurons. To test this, we optogenetically activated BF astrocytes and measured the Ca²⁺ signal from VGLUT2⁺ neurons (Supplementary Fig. S12). As predicted, we found no significant change in the activity of VGLUT2⁺ neurons (Supplementary Fig. S12b, c, $P = 0.09$, Student *t* test). Together, these results suggest that astrocyte activity plays a regulatory role in local neuronal networks; however, such modulation may not lead to substantial changes in neuronal activity.

Astrocyte Ca²⁺ activity in the BF mainly depends on local neuronal activity

Next, we studied the neural mechanisms that caused the astrocyte Ca²⁺ transients in the BF^{42,84}. It has been reported that norepinephrine (NE) released by locus coeruleus (LC) can induce prominent Ca²⁺ activity in

astrocytes in multiple brain regions^{42,50,60,85–88}. However, because we observed a high level of astrocyte Ca²⁺ activity during both wakefulness and REM sleep, and given the fact that LC NE signaling is largely reduced during REM sleep⁸⁹, we thus reasoned that NE signaling might not be a major factor in causing the astrocyte Ca²⁺ transients in the BF during the sleep–wake cycle.

To test this idea, we used prazosin (i.p. injection) to block NE α1 receptors, which are responsible for the NE-induced astrocyte Ca²⁺ signals^{50,86,88}, and measured the changes in astrocyte Ca²⁺ signal in the BF using fiber photometry recording of GCaMP fluorescence in vivo (Supplementary Fig. S13a, b). We found no significant differences in astrocyte Ca²⁺ activity after prazosin application (Supplementary Fig. S13b; $P = 0.91$, Wilcoxon signed-rank test), suggesting that NE is not an important source of the astrocyte Ca²⁺ in the BF.

Another major neuromodulator known to induce Ca²⁺ elevation in astrocytes is acetylcholine (ACh), acting through muscarinic ACh receptors^{42,90–92}, and ACh is also a major neuromodulator in the BF⁹³. We thus tested the contribution of ACh by blocking the muscarinic ACh receptors using atropine (i.p. injection) and found no significant changes in the GCaMP signals after drug injection in vivo (Supplementary Fig. S13c, d; $P = 0.43$, Paired *t*-test).

Lastly, we examined the contribution of local neuronal activity in elevating astrocyte Ca²⁺ signals. We suppressed BF neuronal activity by local infusion of muscimol via an implanted cannula and found that astrocyte Ca²⁺ activity was substantially reduced (Supplementary Fig. S13e, f; $***P < 0.001$, Student's *t*-test). Together, these results suggest that local neuronal activity is the major contributor to the astrocyte Ca²⁺ activity recorded during the sleep–wake cycle.

This conclusion was further supported by our direct recording of astrocyte Ca²⁺ activity (using GCaMP) and

multi-unit neuronal activity in the BF (Fig. 7d–h). The two signals had highly correlated dynamics in both amplitude and time course (Fig. 7f, h; Pearson's $r=0.70$, $***P<0.001$).

There are multiple cell types in the BF^{19,93,94}, including cholinergic neurons, glutamatergic neurons (expressing vesicular glutamate transporter 2, VGLUT2), and GABAergic neurons (expressing vesicular GABA transporter, VGAT), playing distinct roles in the sleep–wake regulation^{18,19,95}. We thus further examined the contribution of these different types of neurons to the observed Ca^{2+} increase in astrocytes during the sleep–wake cycle. Given that we found no critical involvement of the cholinergic muscarinic receptor signaling, we thus focused on the contribution of VGLUT2⁺ neurons and VGAT⁺ neurons.

We first examined the correlation between the Ca^{2+} activity of BF astrocytes and VGLUT2⁺ neurons or VGAT⁺ neurons via simultaneous fiber photometry recording of GCaMP signals using the bilateral dual-probe method in the VGLUT2-Cre or VGAT-Cre mice⁹⁶, respectively (Fig. 7i and Supplementary Fig. S14a, b). We found that both VGLUT2⁺ neurons and VGAT⁺ neurons showed highly correlated Ca^{2+} activity with that in the BF astrocytes (Fig. 7j, k and Supplementary Fig. S14c–h; VGLUT2⁺ neurons vs BF astrocytes: Pearson's $r=0.76$, $***P<0.001$; VGAT⁺ neurons vs BF astrocytes: Pearson's $r=0.80$, $***P<0.001$), and the time difference of astrocyte Ca^{2+} events and the neuronal Ca^{2+} events for both VGLUT2⁺ neurons and VGAT⁺ neurons was close to zero, suggesting that both types of neurons may contribute to the increase of astrocyte Ca^{2+} in the BF.

Notably, we have observed little difference in the rising phase between the population Ca^{2+} signals from astrocytes and neurons in the BF, and this could be due to the limited temporal resolution (1 Hz) of our fiber photometry recording, although the previous study has reported that astrocytes can exhibit rapid Ca^{2+} signal on the timescale similar to neurons⁹⁷. Future studies with single-cell resolution and faster temporal resolution will be needed to further characterize the activity of astrocytes and neurons in the BF.

To further confirm the contribution of these two types of neurons, we optogenetically activated VGLUT2⁺ or VGAT⁺ neurons in the BF using ChrimsonR and measured the evoked astrocyte Ca^{2+} level via fiber photometry recording of GCaMP signals (Fig. 7l and Supplementary Fig. S14i–l). We found that activation of both types of neurons could cause a laser frequency-dependent increase in astrocyte Ca^{2+} level (Fig. 7m, n). Such increase was not caused by non-specific effects of the laser stimulation (e.g., local heating), because laser application in mice without ChrimsonR evoked no detectable change in the astrocyte Ca^{2+} signal

(Supplementary Fig. S7f–h). Together, these results suggest that cell type-specific local neuronal activity in the BF plays a major role in controlling the astrocyte Ca^{2+} activity.

Regulation of sleep–wake cycle by astrocytes in the brainstem

Astrocytes in different brain regions exhibit significant heterogeneity^{6,98}. We thus further examined whether astrocyte Ca^{2+} elevation in other brain regions could also regulate the sleep–wake cycle through similar mechanisms as we observed in the BF.

In the LC/sublaterodorsal nucleus (SLD) region of the brainstem, which is critical for REM sleep regulation^{99,100}, we found that astrocyte Ca^{2+} activity was significantly increased during both wakefulness and REM sleep (Fig. 8a, b and Supplementary Fig. S15a), exhibited rapid changes during brain state transitions (Supplementary Fig. S15b), and was highly correlated with extracellular adenosine levels (Fig. 8a, b and Supplementary Fig. S16), similar to that in the BF. However, the CD73-KO mice showed a comparable level of extracellular adenosine with that in WT mice (Fig. 8c, d; Wake, $P=0.52$; NREM, $P=0.47$; REM, $P=0.22$; Wilcoxon rank-sum test), and the hM₃Dq-induced astrocyte Ca^{2+} elevation caused similar modulation to the sleep–wake behavior in CD73-KO mice and WT mice (Fig. 8e–t and Supplementary Figs. S17 and S18). The most prominent change in the sleep–wake cycle was a reduction in the total time of REM sleep in the hM₃Dq group (Fig. 8f, n; WT was reduced by 41%, $***P=0.0024$; CD73-KO was reduced by 44%, $***P<0.001$). Also diverse modulations to the NREM EEG-Delta power was increased while high-frequency oscillations, including sigma and beta bands, were reduced (Fig. 8j, r; $**P=0.0021$, $***P<0.001$, $***P<0.001$ for delta, sigma, and beta for WT mice; $*P=0.015$, $***P<0.001$, $**P=0.0015$ for CD73-KO mice). These results showed that astrocyte Ca^{2+} elevation in the brainstem might not contribute to extracellular adenosine through the classically proposed ATP-adenosine pathway mediated by CD73, providing further evidence supporting adenosine-independent modulation of the sleep–wake behavior by astrocytes.

Although hM₃Dq-induced astrocyte Ca^{2+} elevation in the LC/SLD also reduced REM sleep as that found in the BF, it appears that this effect was not caused by fragmented NREM sleep because there was no statistical difference in either NREM bout number or bout duration (Fig. 8g, h; bout number, $P=0.42$; bout duration, $P=0.41$). Furthermore, activation of astrocytes in the two brain regions produced opposite modulation of NREM EEG (Figs. 8j and 3l), reducing delta power in the BF but increasing delta power in the LC/SLD. The latter might be caused by the more significant wake-promoting effect of

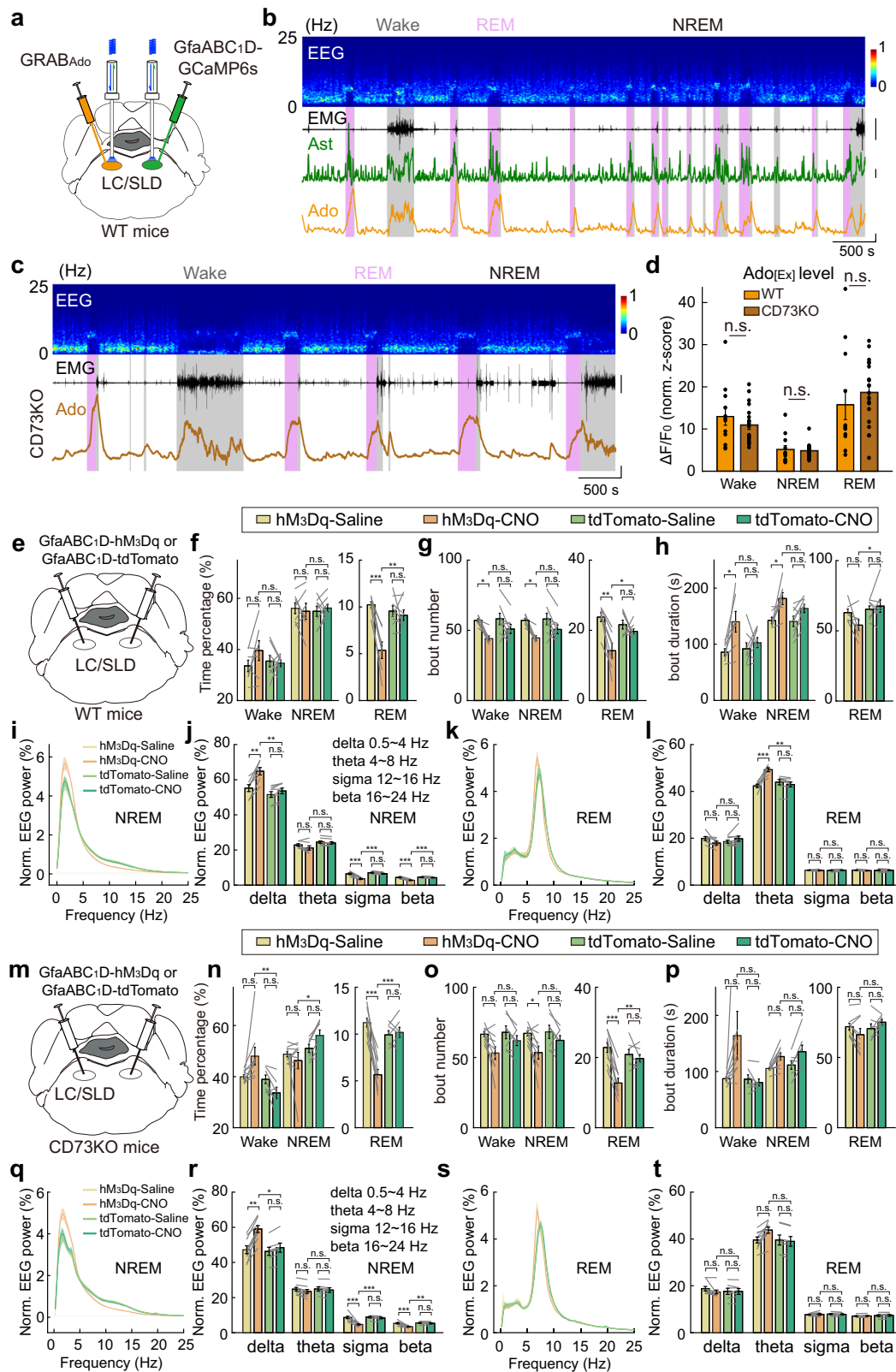


Fig. 8 (See legend on next page.)

(see figure on previous page)

Fig. 8 Sleep–wake regulation by astrocytes in the brainstem. **a** Schematic diagram depicting fiber photometry recording of extracellular adenosine level and population Ca^{2+} signal of astrocytes in LC/SLD region of the brainstem during the sleep–wake cycle. **b** Top to bottom, EEG power spectrogram, EMG (scale, 1 mV), GCaMP fluorescence (scale, 1 z-score), and GRAB_{Ado} fluorescence (scale, 1 z-score). **c** Fiber photometry recording of extracellular adenosine level in LC/SLD in CD73-KO mice during the sleep–wake cycle. **d** GRAB_{Ado} signal in WT and CD73-KO mice in different brain states. Each line represents data from one recording. $n = 12$ sessions from 5 mice in the WT group; $n = 20$ sessions from 6 mice in the CD73-KO group. Wake: $P = 0.52$; NREM: $P = 0.47$; REM: $P = 0.22$; Wilcoxon rank-sum test. **e–l** Same as Fig. 3g–n, respectively, except that experiments were performed in LC/SLD. hM₃Dq group, $n = 7$ mice; tdTomato group, $n = 8$ mice. The statistical method used was two-way repeated measures ANOVA, followed by Tukey's post hoc multiple comparison test. In **f**, hM₃Dq-CNO vs tdTomato-CNO: Wake, $P = 0.47$; NREM, $P = 0.97$; REM, $^{**}P = 0.0024$. hM₃Dq-Saline vs hM₃Dq-CNO: Wake, $P = 0.34$; NREM, $P = 0.98$; REM, $^{***}P < 0.001$. tdTomato-Saline vs tdTomato-CNO: Wake, $P = 0.99$; NREM, $P = 0.97$; REM, $P = 0.94$. In **g**, hM₃Dq-CNO vs tdTomato-CNO: Wake, $P = 0.35$; NREM, $P = 0.42$; REM, $^{*}P = 0.045$. hM₃Dq-Saline vs hM₃Dq-CNO: Wake, $^{*}P = 0.030$; NREM, $^{*}P = 0.034$; REM, $^{**}P = 0.0011$. tdTomato-Saline vs tdTomato-CNO: Wake, $P = 0.27$; NREM, $P = 0.25$; REM, $P = 0.70$. In **h**, hM₃Dq-CNO vs tdTomato-CNO: Wake, $P = 0.12$; NREM, $P = 0.41$; REM, $^{*}P = 0.045$. hM₃Dq-Saline vs hM₃Dq-CNO: Wake, $^{*}P = 0.021$; NREM, $^{*}P = 0.021$; REM, $P = 0.28$. tdTomato-Saline vs tdTomato-CNO: Wake, $P = 0.88$; NREM, $P = 0.19$; REM, $P = 0.95$. In **i**, hM₃Dq-CNO vs tdTomato-CNO: delta, $^{**}P = 0.0021$; theta, $P = 0.088$; sigma, $^{***}P < 0.001$; beta, $^{***}P < 0.001$. hM₃Dq-Saline vs hM₃Dq-CNO: delta, $^{**}P = 0.0085$; theta, $P = 0.46$; sigma, $^{***}P < 0.001$; beta, $^{***}P < 0.001$. tdTomato-Saline vs tdTomato-CNO: delta, $P = 0.81$; theta, $P = 0.97$; sigma, $P = 0.53$; beta, $P = 0.58$. In **l**, hM₃Dq-CNO vs tdTomato-CNO: delta, $P = 0.38$; theta, $^{**}P = 0.0013$; sigma, $P = 0.98$; beta, $P = 0.89$. hM₃Dq-Saline vs hM₃Dq-CNO: delta, $P = 0.36$; theta, $^{***}P < 0.001$; sigma, $P = 0.97$; beta, $P = 0.73$. tdTomato-Saline vs tdTomato-CNO: delta, $P = 0.67$; theta, $P = 0.84$; sigma, $P = 0.93$; beta, $P = 1.0$. **m–t** Same as **e–l**, respectively, except that experiments were performed in CD73-KO mice. hM₃Dq group, $n = 9$ mice; tdTomato group, $n = 7$ mice. The statistical method used was two-way repeated measures ANOVA, followed by Tukey's post hoc multiple comparison test. In **n**, hM₃Dq-CNO vs tdTomato-CNO: Wake, $^{**}P = 0.0020$; NREM, $^{*}P = 0.023$; REM, $^{***}P < 0.001$. hM₃Dq-Saline vs hM₃Dq-CNO: Wake, $P = 0.064$; NREM, $P = 0.80$; REM, $^{***}P < 0.001$. tdTomato-Saline vs tdTomato-CNO: Wake, $P = 0.40$; NREM, $P = 0.40$; REM, $P = 0.98$. In **o**, hM₃Dq-CNO vs tdTomato-CNO: Wake, $P = 0.32$; NREM, $P = 0.34$; REM, $^{**}P = 0.0077$. hM₃Dq-Saline vs hM₃Dq-CNO: Wake, $P = 0.051$; NREM, $^{*}P = 0.050$; REM, $^{***}P < 0.001$. tdTomato-Saline vs tdTomato-CNO: Wake, $P = 0.68$; NREM, $P = 0.67$; REM, $P = 0.93$. In **p**, hM₃Dq-CNO vs tdTomato-CNO: Wake, $P = 0.098$; NREM, $P = 0.80$; REM, $P = 0.23$. hM₃Dq-Saline vs hM₃Dq-CNO: Wake, $P = 0.11$; NREM, $P = 0.12$; REM, $P = 0.53$. tdTomato-Saline vs tdTomato-CNO: Wake, $P = 1.0$; NREM, $P = 0.13$; REM, $P = 0.77$. In **r**, hM₃Dq-CNO vs tdTomato-CNO: delta, $^{*}P = 0.015$; theta, $P = 0.95$; sigma, $^{***}P < 0.001$; beta, $^{**}P = 0.0015$. hM₃Dq-Saline vs hM₃Dq-CNO: delta, $^{**}P = 0.0042$; theta, $P = 0.81$; sigma, $^{***}P < 0.001$; beta, $^{***}P < 0.001$. tdTomato-Saline vs tdTomato-CNO: delta, $P = 0.91$; theta, $P = 0.98$; sigma, $P = 0.90$; beta, $P = 0.96$. In **t**, hM₃Dq-CNO vs tdTomato-CNO: delta, $P = 1.0$; theta, $P = 0.18$; sigma, $P = 1.0$; beta, $P = 0.85$. hM₃Dq-Saline vs hM₃Dq-CNO: delta, $P = 0.72$; theta, $P = 0.22$; sigma, $P = 0.95$; beta, $P = 1.0$. tdTomato-Saline vs tdTomato-CNO: delta, $P = 1.0$; theta, $P = 0.99$; sigma, $P = 0.99$; beta, $P = 0.99$.

astrocyte activation in the LC/SLD, as shown in the time course plot after CNO injection (Supplementary Figs. S3, S9, and S17–S19). Together, these results suggest that astrocyte Ca^{2+} elevation contributes to the sleep–wake behavior through the regulation of the surrounding neural network, thus exhibiting brain region-specific modulations to the sleep–wake cycle¹⁰¹.

Discussion

Using fiber photometry recording of astrocyte Ca^{2+} transients and dynamics in the level of extracellular adenosine and ATP, together with chemogenetic manipulations, optogenetic manipulations, and transgenic mouse model, we provided multiple lines of evidence supporting that astrocytes can modulate the sleep–wake behavior independent of adenosine signaling pathways. Although astrocyte Ca^{2+} transients showed brain state-dependent changes during the sleep–wake cycle (Fig. 2) and had a strong correlation with extracellular adenosine level (Fig. 4b–e), optogenetically evoked Ca^{2+} elevation in BF astrocytes caused no detectable adenosine increase (Supplementary Fig. S6). In the two brain regions critical for sleep–wake control, after genetic deletion of an essential enzyme mediating extracellular ATP-adenosine conversion, there was no detectable effect on the level of extracellular adenosine (Figs. 5a, b and 8c, d), and

elevation of astrocyte Ca^{2+} by chemogenetically activating astrocyte Gq pathway could still significantly modulate the sleep–wake behavior (Figs. 3g–n, 5h–o, and 8e–t). Additionally, directly suppressing astrocyte Ca^{2+} activity in the BF by conditional KO of the IP₃R₂ receptors caused significant modulation of the sleep–wake cycle (Fig. 3s, t and Supplementary Fig. S4c–f); however, no detectable change in the extracellular level of adenosine was observed (Fig. 6e, f). Together, these results strongly suggested that astrocytes could modulate the sleep–wake cycle independent of adenosine signaling pathways.

Astrocytes have long been thought to play a role in sleep–wake regulation^{3,7}. Astrocyte Ca^{2+} activity in multiple brain regions (e.g., cortex and hippocampus) has been reported to show prominent changes during the sleep–wake cycle^{51–54}, and whole animal global reduction of the astrocyte Ca^{2+} activity via genetic ablation of IP₃R₂⁵¹ or the stromal interaction molecule 1 (STIM1)⁵³ altered the sleep–wake behavior. In the current study, we have recorded and manipulated the dynamics of astrocyte Ca^{2+} activity in brain regions that are directly involved in sleep–wake control, providing new data to dissect the cellular mechanisms of sleep–wake modulation by astrocytes.

In the BF, the astrocyte Ca^{2+} activity was primarily generated by local neuronal activity (Supplementary Fig.

S13e, f) but not by neuromodulatory signaling such as NE or Ach (Supplementary Fig. S13a–d), different from that in other brain regions^{42,50,60,80,84,86,87,90–92} or in zebrafish⁸⁸. Such local neuronal activity-dependent astrocyte activity caused a close correlation between neuronal and astrocyte activities (Fig. 7j, k and Supplementary Fig. S14c–h). We have also demonstrated that the Ca²⁺ elevation in BF astrocytes could produce various feedback modulations to the local synaptic transmissions (Fig. 7b, c and Supplementary Fig. S11), which may underlie the astrocyte Ca²⁺ elevation-induced sleep–wake modulation.

The BF is a well-documented brain region that plays a critical role in sleep–wake regulation^{16,18,19}, and neurons in the BF are primarily GABAergic neurons^{102,103} that are more active during wakefulness than during sleep^{19,104}. Our finding of the local neuronal activity-dependent astrocyte activity and the feedback modulation of the local neuronal network by astrocytes suggested that BF astrocytes may amplify the activation of the BF neural network. Because activation of BF neurons mainly promotes wakefulness, thus, the above notion can also explain our results that Ca²⁺ elevation in BF astrocytes decreased the consolidation of NREM sleep (Fig. 3h–n) and suppressing astrocyte Ca²⁺ activity caused more sleep (Fig. 3s, t and Supplementary Fig. S4c–f).

We would like to note that in our chemogenetic manipulation experiments, the careful experimental design by applying multiple pre-habituation trials to the mice and interleaved, multiple experiment sessions for control and CNO injections revealed that low doses of CNO (0.5–1 mg/kg) constantly caused a moderate increase of NREM sleep and decrease of wakefulness in the control group (Figs. 3h, 5i, and 8f, n), a known side effect of CNO^{57,58} that has been largely underestimated in the literature. However, multiple lines of our evidence supported that the major effect that we observed in the experimental groups was likely caused by Ca²⁺ elevation in astrocytes rather than non-specific side effects of CNO: First, CNO-induced modulation in the control groups were generally minor and showed opposite effects compared to the hM₃Dq group; second, the main effect of the chemogenetic manipulation in the hM₃Dq groups were reducing REM sleep, which was not observed in the control groups; third, the use of two-way ANOVA can separately evaluate the contribution of CNO and CNO-induced astrocyte Ca²⁺ elevation, determining the actual effects of astrocyte activation. Moreover, the role of BF astrocytes in sleep–wake regulation was also supported by our loss-of-function manipulation, in which we suppressed the astrocyte Ca²⁺ elevation by the knockout of the IP₃R₂ receptors.

It has been believed that adenosine signaling pathways play a critical role in the sleep–wake modulation by astrocytes, primarily based on studies using the dnSNARE

mice to globally reduce exocytosis in astrocytes and indirect evaluation of the contribution of extracellular adenosine^{3,7,8,105}. However, in these studies, because both neuronal transmissions and gliotransmission of the dnSNARE mice were suppressed by the leaky expression of dnSNARE that was mediated by constitutive GFAP promoter, their observed modulation of sleep–wake behavior cannot be simply attributed to reduced exocytosis in astrocytes. Indeed, decreased neuronal exocytosis could explain the alternation of EEG slow-wave oscillations and the regulation of sleep homeostasis in dnSNARE mice. In our study, using highly specific transgene expressions in astrocytes mediated by AAV5 and GfaABC₁D promoter^{35,36} to bidirectionally manipulate astrocyte Ca²⁺ activity, we demonstrated that brain region-specific astrocyte Ca²⁺ elevation plays a role in regulating the sleep–wake cycle. Importantly, we also measured extracellular levels of ATP and adenosine using genetically encoded novel GRAB sensors while manipulating factors associated with astrocyte-derived adenosine. Removing one of the key enzymes, CD73, that mediates ATP-to-adenosine conversion caused no significant change in adenosine levels in both BF and brain stem, indicating that the CD73-mediated classical pathway does not have a major role in elevating extracellular adenosine levels. However, since other ectoenzymes may also convert ATP to adenosine and the brain region-specific regulation of this pathway is incompletely understood¹⁰⁶, we further examined the contribution of astrocyte-derived ATP by manipulating the intracellular Ca²⁺ levels that control ATP exocytosis. We suppressed astrocyte Ca²⁺ elevation through conditional KO of the IP₃R₂ receptors and found that such manipulation only reduced the amount of ATP but not adenosine. This result strongly suggests that astrocytes have limited contribution in elevating the extracellular level of adenosine^{17,75} in a brain region important for sleep–wake regulation, further indicating that astrocytes can regulate the sleep–wake cycle independent of adenosine signaling pathways. Together, these results provide new insights into the diverse mechanisms in the modulation of the sleep–wake cycle by astrocyte activity. Furthermore, these results provide evidence supporting that neurons, rather than astrocytes, are the primary source of extracellular adenosine^{16,17,75}.

In the current study, our measurements of astrocyte Ca²⁺ activity and the extracellular dynamics of adenosine/ATP were all based on fiber photometry recording, which reports the population signal. Thus, an important question raised by our results is how these activities are spatially organized and related to each other, especially in microdomains of astrocytes^{37,107}. Moreover, we have provided multiple pieces of evidence that strongly suggest that astrocytes may not contribute critically to elevating

the extracellular adenosine level. Thus, they could regulate sleep through adenosine-independent pathways. However, considering the significant heterogeneity of astrocytes in different brain regions^{6,98}, future studies are needed to investigate whether our current findings also apply to other brain regions. Lastly, although our current findings significantly challenge the previous theory that adenosine signaling is key to astrocyte regulation of the sleep–wake cycle, future studies with a complete blockade of astrocyte-derived ATP or other astrocyte sources of adenosine may be needed to further validate our current findings. For example, astrocytes may produce adenosine through IP₃R₂-insensitive ATP release, as IP₃R₂-KO mice still have remaining Ca²⁺ transients in astrocyte processes⁶⁰, which may be important for adenosine generation; astrocytes may also release adenosine directly via transmembrane transporters¹⁰⁸; it is also possible to have Ca²⁺-independent ATP or adenosine release from astrocytes. However, a technical challenge with the complete removal of astrocyte sources of ATP or adenosine is that these manipulations may cause significant abnormality in astrocytes, as both ATP and adenosine are important components of the purinergic pathway that are essential for cell metabolism and survival¹⁰⁹. In addition to these limitations, future studies are also needed to address the alternative cellular mechanisms that underlie astrocyte modulation of the neuronal network in the BF and in other brain regions that are essential for sleep–wake regulation.

Materials and methods

Mice

All experimental procedures have followed the guidelines of the National Institutes of Health and approved by the Animal Care and Use Committee at the Institute of Neuroscience, Chinese Academy of Sciences. Brain slice experiments were performed using young mice (only male mice were used, ~3 weeks at the time of virus injection). In vivo experiments were performed on adult mice (including both genders, > 6 weeks at the time of data collection). Mice were housed in a 12/12-h light/dark cycle (light on at 7 AM) with food and water available ad libitum. Mice with implants for EEG/EMG recording, optogenetic manipulation, or fiber photometry recording were housed individually. WT mice (C57BL/6) were purchased from institute-approved vendors (Shanghai Silaika or LingChang Experiment Animal Co., China). VGAT-IRES-Cre (*Slc32a1*^{tm2(cre)}*Low1*/J, #016962), VGLUT2-IRES-Cre (*Slc17a6*^{tm2(cre)Low1}/J, #016963) and CD73-KO mice (B6.129S1-*Nt5e*^{tm1Lfl}/J, #018986), GFAP-Cre/ERT2 mice (B6.Cg-Tg(GFAP-cre/ERT2)505Fmv/J, #012849), GFAP-Cre (FVB-Tg(GFAP-cre)25Mes/J, #004600), Aldh1l1-Cre (B6;FVB-Tg(Aldh1l1-Cre)JD1884Htz/J, #023748) were obtained from The Jackson Laboratory. IP₃R₂^{flox} mice were kindly shared by

Kunfu Ouyang from Peking University. GFAP-Cre mice were back-crossed to C57BL/6J mice for at least four generations to reduce the FVB strain contribution before usage.

Surgical procedures

All surgical procedures were conducted under general anesthesia using continuous isoflurane (5% for induction; 1.5%–2% for maintenance). Depth of anesthesia was monitored continuously and adjusted when necessary. Following induction of anesthesia, the mice were placed on a stereotaxic frame with a heating pad.

To implant EEG and EMG electrodes, two stainless steel screws for EEG were inserted into the skull above the visual cortex, two other screws were inserted into the skull above the frontal cortex, two insulated EMG electrodes were inserted into the neck muscle, and a reference electrode was attached to a screw inserted into the skull above the cerebellum.

For experiments with virus injection, a craniotomy (~0.5 mm in diameter) was made on top of the BF or LC/SLD, and virus (0.2–0.4 μL) was injected into the BF (AP 0 mm, ML 1.3 mm, DV 5.0 mm from the cortical surface) or LC/SLD (AP –5.6 mm, ML 0.9 mm, DV 3.9 mm from bregma) using Nanoject II (Drummond Scientific) via a glass pipette (23 nL/injection, inter-injection interval 15–30 s). The following AAV viruses were used in current study: AAV2/9-hSyn-GRAB_{Ado1.0} (Addgene vector #153285; titer: 1.5 × 10¹³ or 4.7 × 10¹³ vg/mL; Vigene Biosciences); AAV2/9-GfaABC₁D-GRAB_{Ado1.0} (Addgene vectors #153288; titer: 5 × 10¹² vg/mL; Vigene Biosciences); AAV2/5-GfaABC₁D-cyto-GCaMP6f (Addgene vector #52925; titer: 1.8 × 10¹³ vg/mL; Vigene Biosciences); AAV2/9-GfaABC₁D-GRAB_{ATP1.0} (Addgene vectors #167579; titer: 2.4 × 10¹² vg/mL; BrainVTA Co., China); AAV2/5-GfaABC₁D-hM3Dq-mCherry (Addgene vector #92284; titer: 4.8 × 10¹³ vg/mL; Vigene Biosciences); AAV2/5-GfaABC₁D-tdTomato (Addgene vector #44332, titer: 2.2 × 10¹³ vg/mL; Vigene Biosciences); AAV2/5-GfaABC₁D-ChrimsonR-tdTomato (the plasmid was constructed by Yulong Li's lab; titer: 3 × 10¹³ vg/mL; Vigene Biosciences); AAV2/9-EF1a-DIO-GCaMP6f (titer: 2 × 10¹² vg/mL, BrainVTA Co., China); AAV2/9-hSyn-FLEX-ChrimsonR-tdTomato (titer: 1 × 10¹³ vg/mL, Shanghai Taitool Bioscience Co., China); AAV2/5-GfaABC₁D-cyto-GCaMP6s (gift from Zhifeng Liang's Lab, Titer: 1.8 × 10¹³ vg/mL; Shanghai Taitool Bioscience Co., China); AAV2/5-GfaABC₁D-Cre (titer: 5 × 10¹² vg/mL, BrainVTA Co., China); AAV2/9-EF1a-DIO-hM3Dq-mCherry (titer: 5 × 10¹² vg/mL, BrainVTA Co., China); AAV2/9-CAG-DIO-hM3Dq-mCherry (titer: 5.2 × 10¹² vg/mL, BrainVTA Co., China); AAV2/9-EF1a-DIO-GCaMP6s (titer: 5.2 × 10¹² vg/mL, BrainVTA Co., China); AAV2/8-GfaABC₁D-cyto-

GCaMP6m (titer: 1×10^{13} vg/mL, Shanghai Taitool Bioscience Co., China).

For all the brain slice experiments, AAVs expressing GfaABC₁D-hM3Dq were injected into one hemisphere of the BF, and AAVs expressing GfaABC₁D-tdTomato were injected into the contralateral hemisphere of the BF.

For fiber photometry recording or optogenetic manipulation experiments, a craniotomy (0.5–1 mm in diameter) was made 1–2 weeks after virus injection, and one or two optical fibers (200 μ m in diameter, Thorlabs) with FC ferrule were inserted into the BF or SLD using the same coordinate for virus injection.

For extracellular recording experiments, stereotrodes carried by a lightweight driver were implanted into the BF as described previously¹⁹. The stereotrodes were made by twisting two micro-wires (FeNiCr wires, 25 μ m in diameter, Stablohm 675, California Fine Wire), and the stereotrodes were cut with sharp scissors and electroplated with platinum (H₂PtCl₆, Sigma-Aldrich) to an impedance of \sim 300 k Ω with a lab-made MSP430 MCU-controlled multi-channel plating device.

For the muscimol infusion experiment, an opto-fluid cannula assembly, which allows for precise drug infusion during fiber photometry recording, was implanted into the BF. The cannula consists of two parts, an optical fiber (200 μ m in diameter, Thorlabs) with FC ferrule and an infusion cannula (200 μ m in diameter). The optical fiber and the cannula were glued on a printed circuit board in parallel (500 μ m apart), and the tip of the optical fiber was \sim 500 μ m longer than that of the cannula.

All the implant was secured to the skull using dental cement.

Experiments were carried out at least one week after the last surgery.

Polysomnography recordings

For polysomnography recordings with simultaneous fiber photometry recording or extracellular recording, mice were connected with 1 or 2 optical fibers and a flexible cable for EEG/EMG/multiunit activity. Recordings were made in the home cage placed in a sound-attenuation box (68 cm \times 62 cm \times 74 cm). Each recording session was started after \sim 30 min of habituation and lasted for 1–3 h. The EEG/EMG signals were recorded using a TDT system-3 amplifier (RZ2 + PZ5). EEG/EMG signals were high-pass filtered at 0.5 Hz and digitized at 1525 Hz.

For polysomnography recordings, mice were transferred into recording cages placed in a sound-attenuation box (80 cm \times 100 cm \times 120 cm), connected to the amplifier with a flexible recording cable via a commutator. Three or four mice were recorded simultaneously in one batch, and each batch had both treatment animals and control animals to minimize potential non-specific environmental

influences. Mice were habituated in the recording cage for at least three days before each recording. In the chemo-genetic experiments (Figs. 3g–n, 5h–o, and 8e–t and Supplementary Figs. S3, S9, and S17–S19), mice were recorded for 4 h immediately after each injection (CNO, Tocris Bioscience #4936; 1 mg/kg or 0.5 mg/kg in 50 μ L saline, i.p. injection; or saline, 50 μ L, i.p. injection) starting at 1 PM each day. CNO and saline injections were performed alternately every day for 4–6 days. For the IP₃R₂-KO experiment (Fig. 3r–t and Supplementary Fig. S4), mice were recorded for three days, and the three-day recordings for each mouse were averaged to obtain data for the 24-h sleep–wake cycle.

Fiber photometry recording

To record fluorescence from GCaMP, the adenosine sensor or ATP sensor, we attached an optic fiber (Thorlabs, FT200UMT) to the implanted ferrule via a ceramic sleeve and recorded emission fluorescence using fiber photometry. The photometry rig was constructed using parts from Doric Lens, including a fluorescence optical mini cube (FMC4_AE (405)_E (460–490)_F (500–550)_S), a blue LED (CLED_465), a LED driver (LED_2) and a photoreceiver (NPM_2151_FOA_FC). For recordings containing both green and GCaMP isosbestic channels, an additional LED (CLED_405) was used.

During recording, a software-controlled lock-in detection algorithm was implemented in the TDT RZ2 system using the fiber photometry “Gizmo” of the Synapse software (modulation frequency: 459 Hz for single-channel recording, and 271 or 459 Hz for the second channel in two-channel mode; low-pass filter for demodulated signal: 20 Hz, sixth order). The excitation light intensity was measured as 50–70 μ W (465 nm) or 25–30 μ W (405 nm) from the tip of the optical fiber. The photometry data was stored using a sampling frequency of 1017 Hz.

To minimize the auto-fluorescence of the optical fiber, we bleached the recording fiber before recordings and recorded the reading of background fluorescence intensity. The background fluorescence was subtracted from the recorded signal in subsequent analysis.

For fiber photometry recording during optogenetic activation, we used a photometry rig with a fluorescence optical mini cube (FMC5_E1 (465–480)_F1 (500–540)_E2 (555–570)_F2 (580–680)_S), a LED (CLED_465), a LED driver (LED_2) and a photoreceiver (NPM_2151_FOA_FC). A 638 nm laser was introduced into the light path of the photometry system through the F2 port of the mini cube. To minimize the laser-induced artifact in the photometry signal, we used a 40-Hz square wave to modulate the excitation LED for the photometry recording and applied the laser pulse (power: 10 mW for Fig. 7m, n and Supplementary Figs. S6 and S12; 2 mW for Supplementary Fig. S7c–h; pulse duration: 10 ms) for the optogenetic

stimulation during off period of the photometry LED. The timing of the photometry LED, and laser for the optogenetic stimulation was controlled by the TDT system, which was also used for data acquisition.

Extracellular adenosine levels in the BF and Ca^{2+} activity in astrocytes and neurons show brain state-dependent changes. Thus, to record the adenosine change or Ca^{2+} change directly evoked by the activation of astrocytes or neurons, rather than the indirect adenosine release or Ca^{2+} increase induced by changes in the brain states, we measured the optogenetic-evoked adenosine signal or Ca^{2+} signal under anesthesia (maintained using isoflurane at a concentration of 1.5%; body temperature of the mouse was maintained at 37 °C).

Extracellular recording

Mice were connected with one optical fiber and a flexible cable for EEG/EMG/multiunit activity, and recordings were made in the home cage placed in a sound-attenuation box (68 cm × 62 cm × 74 cm). The stereotrode assembly was moved forward 100 μm in the BF 10 min before each recording. Each recording was started after the mouse fell asleep and lasted for ~1 h.

The EEG/EMG signals and the extracellular signals were recorded using TDT system-3 amplifiers (RZ5 + RA16PA or RZ2 + PZ5). The extracellular signals were filtered at 0.3–8 kHz and sampled at 25 kHz for offline spike detection. Multiunit spiking signals were extracted from the raw data using Offline Sorter (Plexon), and z-score transformed for further analysis.

In vivo pharmacological manipulation

To examine the contribution of acetylcholine or norepinephrine signaling to the astrocyte Ca^{2+} elevation during the sleep–wake cycle, atropine (HY-B0394, MedChemExpress LLC; 5 mg/kg in 100 μL 0.9% NaCl, i.p.) or prazosin (HY-B0193A, MedChemExpress LLC; 1 mg/kg, 10 mg/mL stock in DMSO, diluted with corn oil to 50 μL immediately before use, i.p.) was administered to mice approximately 1.5 h after the start of each recording. Recordings were not interrupted during the i.p. injection. The duration of each recording was ~3 h.

For intracranial muscimol infusion experiments, muscimol (1 mg/mL dissolved in 0.9% NaCl, 200 nL) or saline (200 nL) was infused via an implanted guide cannula. Mice were head-fixed under a dissection microscope, and a microinjection pump was used to deliver the solutions at a speed of 5 nL/s. The infusion cannula was left in place for 5 min before the withdrawal. Immediately after the procedure, mice were returned to the home cage for fiber photometry recordings. Muscimol and saline were infused alternately on different days to minimize non-specific errors (e.g., signal attenuation due to photobleaching).

To examine how chemogenetic activation modulates astrocyte Ca^{2+} signals during the sleep–wake cycle, mice were injected (i.p.) with CNO (1 mg/kg) or saline approximately 1.5 h after the start of each recording. Recordings were not interrupted during the injection and each recording lasted ~3 h.

For each mouse, the power of the excitation light used for the fiber photometry recording remained the same.

Patch-clamp recording in brain slice

Mice were prepared for brain slice recording 2–3 weeks after virus injections as described previously^{19,110–113}. Mice were first injected with CNO (1 mg/kg; dissolved in saline; i.p.), and then were deeply anesthetized with pentobarbital sodium (i.p., 100 mg/kg). After decapitation, the brain was dissected rapidly and placed in ice-cold oxygenated NMDG-HEPES solution (in mM: NMDG 93, KCl 2.5, NaH_2PO_4 1.2, NaHCO_3 30, HEPES 20, D-glucose 25, sodium ascorbate 5, thiourea 2, sodium pyruvate 3, MgSO_4 10 and CaCl_2 0.5, *N*-acetyl-L-cysteine (NAC) 12, at pH 7.4, adjusted with HCl), and coronal slices (with a thickness of 250 μm) containing the BF were made with a vibratome (Leica VT1200S). Brain slices were recovered in oxygenated NMDG-HEPES solution at 32 °C for 10 min and then maintained in an incubation chamber with oxygenated aCSF (in mM: NaCl 124, KCl 4.5, CaCl_2 2, MgCl_2 1, NaHCO_3 26, NaH_2PO_4 1.2, and D-glucose 10) at 25 °C for 1–4 h before recording.

Whole-cell patch-clamp recordings were made using patch pipettes with a resistance of 5–6 MΩ. The recordings were performed using a Multi-Clamp 700B amplifier and pCLAMP10.3 software (Axon Instruments, Molecular Devices). The intracellular solution used for the recording of miniature EPSCs (mEPSCs) and mIPSCs included the following (in mM): CsMeSO₃ 125, CsCl 2, HEPES 10, EGTA 0.5, Mg-ATP 4, Na-GTP 0.3, Na₂-phosphocreatine 10, TEA-Cl 5. The intracellular solution used for tonic GABA recording included the following (in mM): KCl 138, Mg-ATP 4, Na-GTP 0.2, Na₂-phosphocreatine 8, EGTA 1, CaCl_2 0.1, HEPES 10.

For mEPSC recording, neurons were voltage-clamped at –70 mV and pre-incubated with bicuculline (20 μM) and TTX (0.5 μM) for 5 min before recordings. For mIPSC recording, neurons were voltage-clamped at +10 mV and pre-incubated with CNQX (20 μM) and TTX (0.5 μM) for 5 min before recordings. For the recording of tonic GABA currents, SR95531 (20 μM) was bath-applied in the presence of CNQX (10 μM), TTX (1 μM), and APV (25 μM).

All chemicals were purchased from Sigma unless otherwise stated.

Ca^{2+} imaging in brain slice

Coronal slices containing BF were prepared as described above, except that mice were not injected with CNO

before sacrifice. Brain slice was moved to the recording chamber and imaged using a confocal microscope (Fluoview 1000; Olympus) with a 40× water-immersion objective (N.A. = 0.8) at a frame rate of 1 Hz. CNO (1 μ M, Tocris Bioscience #4936) was applied in the bath.

Histology and immunohistochemistry

To verify the virus expression and placements of optical fibers, mice were deeply anesthetized and immediately perfused using 0.1 M phosphate-buffered saline (PBS), followed by 4% paraformaldehyde (PFA). The brain tissues were removed and post-fixed overnight in 4% PFA before dehydration in a 30% sucrose solution. Brain samples were embedded with OCT compound (NEG-50, Thermo Fisher Scientific) and cut into 50 or 40 μ m sections using a cryostat (HM525 NX, Thermo Scientific). Brain sections were stored at -20°C before further processing.

For histology examination, brain sections were washed with PBS and coverslipped using mounting media containing DAPI (H-1500, Vector Labs).

For immunostaining, brain sections were permeabilized using PBST (0.3% Triton X-100 in PBS) for 30 min and incubated with a blocking solution (5% normal goat serum or normal donkey serum) for 1 h before the incubation with a primary antibody overnight at 4°C . The brain sections were then washed with PBS or PBST and incubated with a secondary antibody. Finally, the brain sections were washed and mounted with mounting media.

The following primary or secondary antibodies were used in the current study: chicken anti-GFP (1:500; Aves Labs GFP-1020), rat anti-mCherry (1:500; Thermo Fisher Scientific M11217), rabbit anti-S100 β (1:300; Abcam ab41548), guinea pig anti-NeuN (1:1000; Millipore ABN90), rabbit anti-DsRed (1:500; Takara Bio 632496), rabbit anti-Cre (1:300; Cell Signaling Technology 15036), mouse anti-Cre (1:300; Millipore MAB3120), goat anti-guinea pig Alexa Fluor 647 (1:500; Thermo Fisher Scientific A-21450), donkey anti-chicken Alexa Fluor 488 (1:500; Jackson ImmunoResearch Labs 703-545-155), goat anti-chicken Alexa Fluor 488 (1:1000; Thermo Fisher Scientific A-11039), donkey anti-rabbit Alexa Fluor Cy3 (1:750; Jackson ImmunoResearch Labs 711-165-152), donkey anti-rabbit Alexa Fluor 488 (1:300; Thermo Fisher Scientific A-21206), donkey anti-rat Alexa Fluor 594 (1:500; Thermo Fisher Scientific A-21209), goat anti-mouse Alexa Fluor 647 (1:300; Thermo Fisher Scientific A-21235).

Quantification and statistical analysis

Polysomnography recording analysis

EEG spectral analysis was carried out using a fast Fourier transform (FFT) with a frequency resolution of 0.18 Hz. The brain states were scored every 5 s semi-

automatically in MATLAB and validated manually by trained experimenters. Brain states classification was performed according to established criteria^{16,19}: Wakefulness was defined as desynchronized EEG and high EMG activity; NREM sleep was defined as synchronized EEG with high-amplitude delta activity (0.5–4 Hz) and low EMG activity; REM sleep was defined as high power at theta frequencies (6–10 Hz) and low EMG activity.

Analysis of sleep architecture after chemogenetic manipulation

To analyze changes in the sleep–wake cycle after chemogenetic activation of astrocytes, we used the 4-h polysomnography recording after each injection to calculate the time percentage, bout number, and bout duration of each brain state, and the normalized EEG power spectrum for both NREM and REM sleep. We reported the averaged results for each mouse across multiple injection sessions in Figs. 3g–n, 5h–o, and 8e–t and Supplementary Figs. S3, S9, and S17–S19.

Quantification of virus expression regions in chemogenetic experiments and in 24-h recording test

To quantify the brain regions of AAV-mediated gene expression in the chemogenetic experiments, we processed each brain sample using a standard histology method and imaged brain sections using a slide scanner (VS-120, Olympus). The fluorescence images (AP 0 mm for BF, AP -5.6 mm for LC/LSD) were exported and registered to the Allen Mouse Brain Atlas as described previously^{110,112,113}. We then detected the raw fluorescence signal and normalized the signal using the peak fluorescence intensity of the image. The normalized signal was then averaged across each experimental group to generate the heat map in Supplementary Figs. S3a, b, S4a, b, S9a, b, S17a, and S18a.

Fiber photometry data analysis

To analyze the photometry data, we first binned the raw data into 1 Hz (i.e., down-sampled by 1000) and subtracted the background fluorescence. We then calculated the $\Delta F/F_0$ using a baseline obtained by fitting the background-subtracted data with a second-order exponential function. For fiber photometry recording with both green and the GCaMP isosbestic channels (Fig. 2), we used a MATLAB script “FastICA” to unmix GCaMP signals from physiological artifacts (https://github.com/aludnam/MATLAB/tree/master/FastICA_25).

To identify fast components or remove the slow drift in the photometry signal, we used a MATLAB script “BEADS” (cut-off frequency: adenosine and ATP, 0.00035 cycles/sample; GCaMP, 0.001 cycles/sample) (<https://www.mathworks.com/matlabcentral/fileexchange/49974-beads-baseline-estimation-and-denoising-with-sparsity>).

The z -score transformed $\Delta F/F_0$ was used in the following analysis: (1) The correlation between astrocyte Ca^{2+} signals and GRAB_{Ado} or GRAB_{ATP} signals (Fig. 4c, h and Supplementary Fig. S16a); (2) The correlation between GRAB_{ATP} signals and GRAB_{Ado} signals (Figs. 4m and 5e); (3) The correlation between neuronal Ca^{2+} signals or multiunit activity and astrocyte Ca^{2+} signals (Fig. 7f, j, k); (4) The optogenetic activation-evoked adenosine release or Ca^{2+} increase (Fig. 7m, n and Supplementary Figs. S6c, d, S7c–h, and S12c)

To quantify the change in the adenosine signals, ATP signals, or astrocyte Ca^{2+} signals during the sleep–wake cycle across multiple animals, we further normalized (norm. z -score) the z -score transformed signal ($\Delta F/F_0$) using the standard deviation of these signals during NREM sleep when there was no apparent fluctuation in the signal. The normalized $\Delta F/F_0$ was used for the analysis in Figs. 2c–f, 3f, q, 5b, 6c, f, and 8d and Supplementary Fig. S15.

To analyze the correlation between astrocyte Ca^{2+} activity and movement, we first selected a recording with prolonged wakefulness, and then used behavioral movies to distinguish between “Locomotion” and “Quiet wakefulness”. During the locomotion period, the mice were often walking and running, in contrast to the typical behaviors, including immobility, grooming, scratching, and sniffing during the quiet wakefulness. The duration of each segment was 10–60 s.

To quantify the change in astrocyte Ca^{2+} signals after i.p. injection of atropine or prazosin, we first extracted the GCaMP events that were larger than twice the standard deviation of the signal, and then defined the mean amplitude of these events as the size of GCaMP signals. We used the size of GCaMP signals before drug applications and 10 min after drug applications to evaluate the effects of the drugs. The same method was used to calculate the size of GCaMP signals after intracranial infusion of muscimol or saline.

To quantify the change in astrocyte Ca^{2+} signal following chemogenetic activation, we first used a MATLAB function “findpeaks” to extract GCaMP events greater than twice the standard deviation of the signal from the tdTomato-expressing BF, and calculated the ratio between events from the tdTomato-expressing BF and the corresponding events from the hM_3Dq -expressing BF. We then calculated the average ratio before and after CNO or saline injections (2 min to 1 h post injection) for each recording. This ratio was used to quantify the CNO-induced changes.

To quantify the change in astrocyte Ca^{2+} signal following KO of IP_3R_2 receptors, we first used a MATLAB function “findpeaks” to extract GCaMP events greater than twice the standard deviation of the signal from the Cre-expressing BF and then used them to determine the

corresponding events from the tdTomato-expressing BF. We then calculated the mean amplitude of events from the Cre-expressing BF and tdTomato-expressing BF for each brain state. Normalized amplitudes were used to assess the effect of IP_3R_2 KO.

We found that the fluorescence signals at the beginning of each recording (~ 10 min) were often subjected to a faster decline, which might be caused by photobleaching of the auto-fluorescence in the brain tissue. We thus removed data during this period in the quantification.

Analysis of the correlation between two signals

To analyze the correlation and time course relationship between two signals in Figs. 4c–e, h–j, m–o, 5e–g, and 7f–h, j, k and Supplementary Figs. S14e–h and S16, we selected events in the GRAB_{Ado} signal (Figs. 4c–e, m–o and 5e–g and Supplementary Fig. S16), GRAB_{ATP} signal (Fig. 4h–j), or astrocyte Ca^{2+} signal (Fig. 7f–h, j, k; Supplementary Fig. S14e–h) and defined the event onset or offset as the time when the signal increased above 10% of its peak amplitude in the rising edge or decreased under 10% of the peak amplitude in the falling edge, respectively. We used the onset or offset time as a reference to align the two signals and calculated a peri-event time histogram (PETH). The PETH was further normalized (0–1) to get the plots in Figs. 4e, j, o, 5g, and 7h and Supplementary Figs. S14f, h and S16c. We defined the C_{50} of the PETH as the time when the signal passed half of its peak amplitude and used the difference in C_{50} between the two signals to estimate the averaged difference in the time course of the two signals. The Σ_{flour} (i.e., area under a curve, AUC) of a selected event (relative to a baseline defined as the mean of the signal during the 100 s period before the onset of each event) was used to generate the scatter plot in Figs. 4c, h, m, 5e, and 7f, j, k and Supplementary Fig. S16a. Due to the difference in the time course between the two signals, we subtracted the onset and offset time of the GRAB_{Ado} events (Figs. 4c, m and 5e and Supplementary Fig. S16a), GRAB_{ATP} (Fig. 4h), or astrocyte Ca^{2+} events (Fig. 7f, j, k) by the time difference in the C_{50} of the PETH of the two signals and used the shifted onset and offset time to calculate the AUC. To estimate the non-specific correlation between the two signals, we randomly shuffled the astrocyte Ca^{2+} signals (Fig. 4d, i and Supplementary Fig. S16b), the GRAB_{ATP} signals (Figs. 4n, 5f), or the neuronal Ca^{2+} signals (Fig. 7g and Supplementary Fig. S14e, g) and calculated the AUC using the same method as in the non-shuffled condition to get the scatter plot in Figs. 4d, i, n, 5f, and 7g and Supplementary Figs. S14e, g and S16b.

Analysis of Ca^{2+} imaging in brain slice

Analysis of time-lapse image series was performed in MATLAB similar to that described previously³⁶. We first

corrected the drift of the images using a rigid-affine algorithm in ANTs (<http://stnava.github.io/ANTs/>) and extracted Ca^{2+} signals using CNMF-E (https://github.com/zhoup/CNMF_E). The Ca^{2+} signal was then normalized to the global background estimated in CNMF-E and used to calculate the AUC of each Ca^{2+} event. To quantify the effect of CNO on astrocyte Ca^{2+} signal, we calculated the average size of the Ca^{2+} event during the 120 s before and after CNO application and generate data for Fig. 3c.

Analysis of patch-clamp recording in brain slice

The mEPSCs and mIPSCs were extracted using the Mini Analysis Program (Synaptosoft). The tonic GABA current was analyzed using the Clampfit software (Molecular Devices). We manually selected the recording period before and after the application of SR95521, and used the shift in the averaged current to calculate the tonic GABA current.

Statistical tests

Statistic procedures We first performed a normality test on each dataset using the Shapiro–Wilk test. Parametric tests (paired or unpaired Student's *t*-tests) were used if the dataset was normally distributed ($P < 0.05$), otherwise non-parametric tests (Wilcoxon signed-rank test or Wilcoxon rank-sum test) were used. Multiple group comparisons (Figs. 3g–n, 5h–o, and 8e–t and Supplementary Figs. S3, S9, S17–S19) were performed by two-way repeated measures ANOVA, followed by Tukey's post hoc multiple comparison test. All the statistical tests were two-tailed and performed in MATLAB or OriginPro 2019b. The significance level was set at $P = 0.05$.

Sample size We did not perform a calculation on the sample size. We used a sample size comparable to studies using similar techniques and animal models.

Data exclusion criteria Mice in the chemogenetic experiments and fiber photometry experiments were excluded based on post-hoc verification of the virus expression or the placement of the optical fiber.

The investigators were not blinded to the genotypes or the experimental conditions of the animals.

Acknowledgements

We thank Dr. M. Poo for his critical reading of the manuscript; Dr. Y. Dan and Dr. A. Adamantidis for comments or suggestions; Z. Tao, Z. Xiao, K. Song, D. Liu, Y. Hu and Y. Pan for technical assistant; Dr. K. Ouyang and Dr. F. Huang for sharing the $\text{IP}_3\text{R}_2^{\text{fllox}}$ mice. This work was supported by the "Strategic Priority Research Program" of the Chinese Academy of Sciences (XDB32010000 to M.X.), grants from the National Natural Science Foundation of China (32221003 and 31871074 to M.X., 31925017 to Y.L., 32170993 to S.Z., 31900711 to G.M.), National Key R&D Program of China (2017YFE0196600 to M.X., 2020YFE0204000 to Y.L.), CAS Project for Young Scientists in Basic Research (YSBR-071 to M.X.), Lingang Laboratory & National Key Laboratory of Human

Factors Engineering Joint Grant (LG-TKN-202203-01 to M.X.), National Science and Technology Innovation 2030 Major Program (2021ZD0203704 and 2021ZD0202804 to S.Z.), Key Laboratory of Cell Differentiation and Apoptosis of the Chinese Ministry of Education (S.Z.), the innovative research team of high-level local universities in Shanghai (S.Z.), Shanghai Municipal Science and Technology Major Project (2018SHZDZX05 and 2021SHZDZX to M.X.), Shanghai Post-doctoral Excellence Program (2021399 to W.P.), Postdoctoral Innovative Talents Supporting Program (W.P.), China Postdoctoral Science Foundation (W.P.), Special Research Assistant Project of the Chinese Academy of Sciences (W.P.), funding from Shanghai Municipal Science and Technology (21ZR1436400 to S.Z.), the Feng Foundation of Biomedical Research (Y.L.). Z.Wu. is supported by the Boehringer Ingelheim-Peking University Postdoctoral Program.

Author details

¹Institute of Neuroscience, State Key Laboratory of Neuroscience, CAS Center for Excellence in Brain Science and Intelligence Technology, Chinese Academy of Sciences, Shanghai, China. ²University of Chinese Academy of Sciences, Beijing, China. ³Center for Brain Science of Shanghai Children's Medical Center, Department of Anatomy and Physiology, Shanghai Jiao Tong University School of Medicine, Shanghai, China. ⁴Songjiang Institute and Songjiang Hospital, Shanghai Jiao Tong University School of Medicine, Shanghai, China. ⁵State Key Laboratory of Membrane Biology, Peking University School of Life Sciences, Beijing, China. ⁶Peking-Tsinghua Center for Life Sciences, Academy for Advanced Interdisciplinary Studies, Peking University, Beijing, China. ⁷PKU-IDG/McGovern Institute for Brain Research, Beijing, China. ⁸Shanghai Center for Brain Science and Brain-Inspired Intelligence Technology, Shanghai, China

Author contributions

M.X. conceived and supervised the projects; G.M. performed the experiments using brain slice preparation; All other experiments were performed by W.P., X.L., Z. Wang, and X.F. with assistance by M.Q. and L.W.; The data from brain slice experiments were analyzed by G.M., and all other data were analyzed by W.P., S.Z., and M.X.; Z.Wu developed the GRAB_{add} and GRAB_{ATP} sensors under the supervision of Y.L.; All authors contributed to data interpretation; M.X. and S.Z. wrote the manuscript with inputs from all other authors.

Data availability

The data supporting the findings of this study are included in the figures and supporting files. The raw data are available from the corresponding author upon request.

Conflict of interest

The authors declare no competing interests.

Publisher's note

Springer Nature remains neutral with regard to jurisdictional claims in published maps and institutional affiliations.

Supplementary information The online version contains supplementary material available at <https://doi.org/10.1038/s41421-022-00498-9>.

Received: 13 March 2022 Accepted: 20 November 2022

Published online: 07 February 2023

References

1. von Bartheld, C. S., Bahney, J. & Herculano-Houzel, S. The search for true numbers of neurons and glial cells in the human brain: A review of 150 years of cell counting. *J. Comp. Neurol.* **524**, 3865–3895 (2016).
2. Nedergaard, M., Ransom, B. & Goldman, S. A. New roles for astrocytes: redefining the functional architecture of the brain. *Trends Neurosci.* **26**, 523–530 (2003).
3. Halassa, M. M. & Haydon, P. G. Integrated brain circuits: astrocytic networks modulate neuronal activity and behavior. *Annu. Rev. Physiol.* **72**, 335–355 (2010).
4. Sofroniew, M. V. & Vinters, H. V. Astrocytes: biology and pathology. *Acta Neuropathol.* **119**, 7–35 (2010).

5. Santello, M., Toni, N. & Volterra, A. Astrocyte function from information processing to cognition and cognitive impairment. *Nat. Neurosci.* **22**, 154–166 (2019).
6. Khakh, B. S. & Sofroniew, M. V. Diversity of astrocyte functions and phenotypes in neural circuits. *Nat. Neurosci.* **18**, 942–952 (2015).
7. Haydon, P. G. Astrocytes and the modulation of sleep. *Curr. Opin. Neurobiol.* **44**, 28–33 (2017).
8. Halassa, M. M. et al. Astrocytic modulation of sleep homeostasis and cognitive consequences of sleep loss. *Neuron* **61**, 213–219 (2009).
9. Fellin, T. et al. Endogenous nonneuronal modulators of synaptic transmission control cortical slow oscillations in vivo. *Proc. Natl. Acad. Sci. USA* **106**, 15037–15042 (2009).
10. Nadjar, A., Blutstein, T., Aubert, A., Laye, S. & Haydon, P. G. Astrocyte-derived adenosine modulates increased sleep pressure during inflammatory response. *Glia* **61**, 724–731 (2013).
11. Pascual, O. et al. Astrocytic purinergic signaling coordinates synaptic networks. *Science* **310**, 113–116 (2005).
12. Zhuo, L. et al. hGFAP-cre transgenic mice for manipulation of glial and neuronal function in vivo. *Genesis* **31**, 85–94 (2001).
13. Su, M. et al. Expression Specificity of GFAP Transgenes. *Neurochem. Res.* **29**, 2075–2093 (2004).
14. Yu, X., Nagai, J. & Khakh, B. S. Improved tools to study astrocytes. *Nat. Rev. Neurosci.* **21**, 121–138 (2020).
15. Camici, M., Garcia-Gil, M. & Tozzi, M. G. The inside story of adenosine. *Int. J. Mol. Sci.* **19**, 784 (2018).
16. Peng, W. et al. Regulation of sleep homeostasis mediator adenosine by basal forebrain glutamatergic neurons. *Science* **369**, eabb0556 (2020).
17. Lovatt, D. et al. Neuronal adenosine release, and not astrocytic ATP release, mediates feedback inhibition of excitatory activity. *Proc. Natl. Acad. Sci. USA* **109**, 6265–6270 (2012).
18. Anaclet, C. et al. Basal forebrain control of wakefulness and cortical rhythms. *Nat. Commun.* **6**, 8744 (2015).
19. Xu, M. et al. Basal forebrain circuit for sleep-wake control. *Nat. Neurosci.* **18**, 1641–1647 (2015).
20. Porkka-Heiskanen, T. et al. Adenosine: a mediator of the sleep-inducing effects of prolonged wakefulness. *Science* **276**, 1265–1268 (1997).
21. Basheer, R., Strecker, R. E., Thakkar, M. M. & McCarley, R. W. Adenosine and sleep-wake regulation. *Prog. Neurobiol.* **73**, 379–396 (2004).
22. Greene, R. W., Bjorness, T. E. & Suzuki, A. The adenosine-mediated, neuronal-glial, homeostatic sleep response. *Curr. Opin. Neurobiol.* **44**, 236–242 (2017).
23. Ganat, Y. M. et al. Early postnatal astroglial cells produce multilineage precursors and neural stem cells in vivo. *J. Neurosci.* **26**, 8609–8621 (2006).
24. Tien, A. C. et al. Regulated temporal-spatial astrocyte precursor cell proliferation involves BRAF signalling in mammalian spinal cord. *Development* **139**, 2477–2487 (2012).
25. Bellesi, M., de Vivo, L., Tononi, G. & Cirelli, C. Effects of sleep and wake on astrocytes: clues from molecular and ultrastructural studies. *BMC Biol.* **13**, 66 (2015).
26. Lozzi, B., Huang, T. W., Sardar, D., Huang, A. Y. & Deneen, B. Regionally distinct astrocytes display unique transcription factor profiles in the adult brain. *Front. Neurosci.* **14**, 61 (2020).
27. Xin, W. et al. Ventral midbrain astrocytes display unique physiological features and sensitivity to dopamine D2 receptor signaling. *Neuropsychopharmacology* **44**, 344–355 (2019).
28. Yang, Y. et al. Molecular comparison of GLT1 + and ALDH1L1 + astrocytes in vivo in astroglial reporter mice. *Glia* **59**, 200–207 (2011).
29. Park, Y. M., Chun, H., Shin, J. I. & Lee, C. J. Astrocyte specificity and coverage of hGFAP-CreERT2 [Tg(GFAPCre/ERT2)13Kdmc] mouse line in various brain regions. *Exp. Neurobiol.* **27**, 508–525 (2018).
30. Casper, K. B., Jones, K. & McCarthy, K. D. Characterization of astrocyte-specific conditional knockouts. *Genesis* **45**, 292–299 (2007).
31. Chow, L. M., Zhang, J. & Baker, S. J. Inducible Cre recombinase activity in mouse mature astrocytes and adult neural precursor cells. *Transgenic Res.* **17**, 919–928 (2008).
32. Hirrlinger, P. G., Scheller, A., Braun, C., Hirrlinger, J. & Kirchhoff, F. Temporal control of gene recombination in astrocytes by transgenic expression of the tamoxifen-inducible DNA recombinase variant CreERT2. *Glia* **54**, 11–20 (2006).
33. Brenner, M. & Messing, A. GFAP transgenic mice. *Methods* **10**, 351–364 (1996).
34. Hu, N. Y. et al. Expression patterns of inducible Cre recombinase driven by differential astrocyte-specific promoters in transgenic mouse lines. *Neurosci. Bull.* **36**, 530–544 (2020).
35. Nagai, J. et al. Hyperactivity with disrupted attention by activation of an astrocyte synaptogenic cue. *Cell* **177**, 1280.e20–1292.e20 (2019).
36. Yu, X. et al. Reducing astrocyte calcium signaling in vivo alters striatal microcircuits and causes repetitive behavior. *Neuron* **99**, 1170–1187.e9 (2018).
37. Shigetomi, E. et al. Imaging calcium microdomains within entire astrocyte territories and endfeet with GCaMPs expressed using adeno-associated viruses. *J. Gen. Physiol.* **141**, 633–647 (2013).
38. Ortinski, P. I. et al. Selective induction of astrocytic gliosis generates deficits in neuronal inhibition. *Nat. Neurosci.* **13**, 584–591 (2010).
39. Xie, Y., Wang, T., Sun, G. Y. & Ding, S. Specific disruption of astrocytic Ca²⁺ signaling pathway in vivo by adeno-associated viral transduction. *Neuroscience* **170**, 992–1003 (2010).
40. Huang, H., He, W., Tang, T. & Qiu, M. Immunological markers for central nervous system glia. *Neurosci. Bull.* <https://doi.org/10.1007/s12264-022-00938-2> (2022).
41. Shigetomi, E., Patel, S. & Khakh, B. S. Probing the complexities of astrocyte calcium signaling. *Trends Cell Biol.* **26**, 300–312 (2016).
42. Bazargani, N. & Attwell, D. Astrocyte calcium signaling: the third wave. *Nat. Neurosci.* **19**, 182–189 (2016).
43. Chen, T. W. et al. Ultrasensitive fluorescent proteins for imaging neuronal activity. *Nature* **499**, 295–300 (2013).
44. Hausteiner, M. D. et al. Conditions and constraints for astrocyte calcium signaling in the hippocampal mossy fiber pathway. *Neuron* **82**, 413–429 (2014).
45. Kim, C. K. et al. Simultaneous fast measurement of circuit dynamics at multiple sites across the mammalian brain. *Nat. Methods* **13**, 325–328 (2016).
46. Tian, L. et al. Imaging neural activity in worms, flies and mice with improved GCaMP calcium indicators. *Nat. Methods* **6**, 875–881 (2009).
47. Qin, H. et al. Monitoring astrocytic Ca²⁺ activity in freely behaving mice. *Front. Cell. Neurosci.* **14**, 603095 (2020).
48. Dombeck, D. A., Khabbaz, A. N., Collman, F., Adelman, T. L. & Tank, D. W. Imaging large-scale neural activity with cellular resolution in awake, mobile mice. *Neuron* **56**, 43–57 (2007).
49. Nimmerjahn, A., Mukamel, E. A. & Schnitzer, M. J. Motor behavior activates Bergmann glial networks. *Neuron* **62**, 400–412 (2009).
50. Paukert, M. et al. Norepinephrine controls astroglial responsiveness to local circuit activity. *Neuron* **82**, 1263–1270 (2014).
51. Bojarskaite, L. et al. Astrocytic Ca²⁺ signaling is reduced during sleep and is involved in the regulation of slow wave sleep. *Nat. Commun.* **11**, 3240 (2020).
52. Vaidyanathan, T. V., Collard, M., Yokoyama, S., Reitman, M. E. & Poskanzer, K. E. Cortical astrocytes independently regulate sleep depth and duration via separate GPCR pathways. *Elife* **10**, e63329 (2021).
53. Ingiosi, A. M. et al. A role for astroglial calcium in mammalian sleep and sleep regulation. *Curr. Biol.* **30**, 4373–4383.e7 (2020).
54. Tsunematsu, T., Sakata, S., Sanagi, T., Tanaka, K. F. & Matsui, K. Region-specific and state-dependent astrocyte Ca²⁺ dynamics during the sleep-wake cycle in mice. *J. Neurosci.* **41**, 5440–5452 (2021).
55. Chai, H. et al. Neural circuit-specialized astrocytes: transcriptomic, proteomic, morphological, and functional evidence. *Neuron* **95**, 531–549.e9 (2017).
56. Roth, B. L. DREADDs for neuroscientists. *Neuron* **89**, 683–694 (2016).
57. Gomez, J. L. et al. Chemogenetics revealed: DREADD occupancy and activation via converted clozapine. *Science* **357**, 503–507 (2017).
58. Manvich, D. F. et al. The DREADD agonist clozapine N-oxide (CNO) is reverse-metabolized to clozapine and produces clozapine-like interoceptive stimulus effects in rats and mice. *Sci. Rep.* **8**, 3840 (2018).
59. Li, X., Zima, A. V., Sheikh, F., Blatter, L. A. & Chen, J. Endothelin-1-induced arrhythmogenic Ca²⁺ signaling is abolished in atrial myocytes of inositol-1,4,5-trisphosphate(IP3)-receptor type 2-deficient mice. *Circ. Res.* **96**, 1274–1281 (2005).
60. Srinivasan, R. et al. Ca²⁺ signaling in astrocytes from Ipr3r2(-/-) mice in brain slices and during startle responses in vivo. *Nat. Neurosci.* **18**, 708–717 (2015).
61. van der Mierden, S., Savelyev, S. A., Int'Hout, J., de Vries, R. B. M. & Leenaars, C. H. C. Intracerebral microdialysis of adenosine and adenosine monophosphate—a systematic review and meta-regression analysis of baseline concentrations. *J. Neurochem.* **147**, 58–70 (2018).
62. Fredholm, B. B. Adenosine—a physiological or pathophysiological agent? *J. Mol. Med.* **92**, 201–206 (2014).

63. Wu, Z. et al. A sensitive GRAB sensor for detecting extracellular ATP in vitro and in vivo. *Neuron* **110**, 770.e5–782.e5 (2021).
64. Wu, Z. et al. A GRAB sensor reveals activity-dependent non-vesicular somatodendritic adenosine release. *bioRxiv* <https://doi.org/10.1101/2020.05.04.075564> (2020).
65. Fields, R. D. & Burnstock, G. Purinergic signalling in neuron-glia interactions. *Nat. Rev. Neurosci.* **7**, 423–436 (2006).
66. Zhang, J. M. et al. ATP released by astrocytes mediates glutamatergic activity-dependent heterosynaptic suppression. *Neuron* **40**, 971–982 (2003).
67. Klapoetke, N. C. et al. Independent optical excitation of distinct neural populations. *Nat. Methods* **11**, 338–346 (2014).
68. Savtchouk, I. & Volterra, A. Gliotransmission: beyond black-and-white. *J. Neurosci.* **38**, 14–25 (2018).
69. Fiacco, T. A. & McCarthy, K. D. Multiple lines of evidence indicate that gliotransmission does not occur under physiological conditions. *J. Neurosci.* **38**, 3–13 (2018).
70. Langer, D. et al. Distribution of ectonucleotidases in the rodent brain revisited. *Cell Tissue Res.* **334**, 199–217 (2008).
71. Zimmermann, H. Biochemistry localization and functional roles of ectonucleotidases in the nervous system. *Prog. Neurobiol.* **49**, 589–618 (1996).
72. Kuleshkaya, N. et al. CD73 is a major regulator of adenosinergic signalling in mouse brain. *PLoS ONE* **8**, e66896 (2013).
73. Thompson, L. F. et al. Crucial role for ecto-5'-nucleotidase (CD73) in vascular leakage during hypoxia. *J. Exp. Med.* **200**, 1395–1405 (2004).
74. Goswami, S. et al. Immune profiling of human tumors identifies CD73 as a combinatorial target in glioblastoma. *Nat. Med.* **26**, 39–46 (2020).
75. Wall, M. & Dale, N. Activity-dependent release of adenosine: a critical re-evaluation of mechanism. *Curr. Neuropharmacol.* **6**, 329–337 (2008).
76. Mitchell, J. B., Lupica, C. R. & Dunwiddie, T. V. Activity-dependent release of endogenous adenosine modulates synaptic responses in the rat hippocampus. *J. Neurosci.* **13**, 3439–3447 (1993).
77. Butt, A. M. ATP: a ubiquitous gliotransmitter integrating neuron-glia networks. *Semin. Cell Dev. Biol.* **22**, 205–213 (2011).
78. Newman, E. A. New roles for astrocytes: regulation of synaptic transmission. *Trends Neurosci.* **26**, 536–542 (2003).
79. Dallerac, G., Chever, O. & Rouach, N. How do astrocytes shape synaptic transmission? Insights from electrophysiology. *Front. Cell. Neurosci.* **7**, 159 (2013).
80. Lines, J., Martin, E. D., Kofuji, P., Aguilar, J. & Araque, A. Astrocytes modulate sensory-evoked neuronal network activity. *Nat. Commun.* **11**, 3689 (2020).
81. Lee, S. et al. Channel-mediated tonic GABA release from glia. *Science* **330**, 790–796 (2010).
82. Jo, S. et al. GABA from reactive astrocytes impairs memory in mouse models of Alzheimer's disease. *Nat. Med.* **20**, 886–896 (2014).
83. Kwak, H. et al. Astrocytes control sensory acuity via tonic inhibition in the thalamus. *Neuron* **108**, 691–706 e610 (2020).
84. Volterra, A., Liaudet, N. & Savtchouk, I. Astrocyte Ca(2+) signalling: an unexpected complexity. *Nat. Rev. Neurosci.* **15**, 327–335 (2014).
85. Bekar, L. K., He, W. & Nedergaard, M. Locus coeruleus alpha-adrenergic-mediated activation of cortical astrocytes in vivo. *Cereb. Cortex* **18**, 2789–2795 (2008).
86. Ding, F. et al. alpha1-Adrenergic receptors mediate coordinated Ca2+ signaling of cortical astrocytes in awake, behaving mice. *Cell Calcium* **54**, 387–394 (2013).
87. Kjaerby, C., Rasmussen, R., Andersen, M. & Nedergaard, M. Does global astrocytic calcium signaling participate in awake brain state transitions and neuronal circuit function? *Neurochem. Res.* **42**, 1810–1822 (2017).
88. Mu, Y. et al. Glia accumulate evidence that actions are futile and suppress unsuccessful behavior. *Cell* **178**, 27–43 e19 (2019).
89. Aston-Jones, G. & Bloom, F. E. Activity of norepinephrine-containing locus coeruleus neurons in behaving rats anticipates fluctuations in the sleep-wake cycle. *J. Neurosci.* **1**, 876–886 (1981).
90. Takata, N. et al. Astrocyte calcium signaling transforms cholinergic modulation to cortical plasticity in vivo. *J. Neurosci.* **31**, 18155–18165 (2011).
91. Chen, N. et al. Nucleus basalis-enabled stimulus-specific plasticity in the visual cortex is mediated by astrocytes. *Proc. Natl. Acad. Sci. USA* **109**, E2832–E2841 (2012).
92. Navarrete, M. et al. Astrocytes mediate in vivo cholinergic-induced synaptic plasticity. *PLoS Biol.* **10**, e1001259 (2012).
93. Zaborszky, L. The modular organization of brain systems. Basal forebrain: the last frontier. *Prog. Brain Res.* **136**, 359–372 (2002).
94. Manns, I. D., Alonso, A. & Jones, B. E. Rhythmically discharging basal forebrain units comprise cholinergic, GABAergic, and putative glutamatergic cells. *J. Neurophysiol.* **89**, 1057–1066 (2003).
95. Yang, C., Thankachan, S., McCarley, R. W. & Brown, R. E. The menagerie of the basal forebrain: how many (neural) species are there, what do they look like, how do they behave and who talks to whom? *Curr. Opin. Neurobiol.* **44**, 159–166 (2017).
96. Vong, L. et al. Leptin action on GABAergic neurons prevents obesity and reduces inhibitory tone to POMC neurons. *Neuron* **71**, 142–154 (2011).
97. Stobart, J. L. et al. Cortical circuit activity evokes rapid astrocyte calcium signals on a similar timescale to neurons. *Neuron* **98**, 726.e4–735.e4 (2018).
98. Zhang, Y. & Barres, B. A. Astrocyte heterogeneity: an underappreciated topic in neurobiology. *Curr. Opin. Neurobiol.* **20**, 588–594 (2010).
99. Luppi, P. H. et al. Brainstem mechanisms of paradoxical (REM) sleep generation. *Pflug. Arch.* **463**, 43–52 (2012).
100. Lu, J., Sherman, D., Devor, M. & Saper, C. B. A putative flip-flop switch for control of REM sleep. *Nature* **441**, 589–594 (2006).
101. Theodosis, D. T., Poulain, D. A. & Olliet, S. H. Activity-dependent structural and functional plasticity of astrocyte-neuron interactions. *Physiol. Rev.* **88**, 983–1008 (2008).
102. Gritti, I. et al. Stereological estimates of the basal forebrain cell population in the rat, including neurons containing choline acetyltransferase, glutamic acid decarboxylase or phosphate-activated glutaminase and colocalizing vesicular glutamate transporters. *Neuroscience* **143**, 1051–1064 (2006).
103. Zaborszky, L., Pol, A. van den & Gyengesi, E. in *The Mouse Nervous System* (eds G. Paxinos, G. & Puelles, L.) 684–718 (Elsevier, 2012).
104. Hassani, O. K., Lee, M. G., Henny, P. & Jones, B. E. Discharge profiles of identified GABAergic in comparison to cholinergic and putative glutamatergic basal forebrain neurons across the sleep-wake cycle. *J. Neurosci.* **29**, 11828–11840 (2009).
105. Fujita, T. et al. Neuronal transgene expression in dominant-negative SNARE mice. *J. Neurosci.* **34**, 16594–16604 (2014).
106. Yegutkin, G. G. Nucleotide- and nucleoside-converting ectoenzymes: Important modulators of purinergic signalling cascade. *Biochim. Biophys. Acta* **1783**, 673–694 (2008).
107. Khakh, B. S. & McCarthy, K. D. Astrocyte calcium signaling: from observations to functions and the challenges therein. *Cold Spring Harb. Perspect. Biol.* **7**, a020404 (2015).
108. Baldwin, S. A. et al. The equilibrative nucleoside transporter family, SLC29. *Pflug. Arch.* **447**, 735–743 (2004).
109. Burnstock, G. Physiology and pathophysiology of purinergic neurotransmission. *Physiol. Rev.* **87**, 659–797 (2007).
110. Zhang, S. et al. Organization of long-range inputs and outputs of frontal cortex for top-down control. *Nat. Neurosci.* **19**, 1733–1742 (2016).
111. Zhang, S. et al. Selective attention. Long-range and local circuits for top-down modulation of visual cortex processing. *Science* **345**, 660–665 (2014).
112. Do, J. P. et al. Cell type-specific long-range connections of basal forebrain circuit. *Elife* **5**, e13214 (2016).
113. Ma, G. et al. Hierarchy in sensory processing reflected by innervation balance on cortical interneurons. *Sci. Adv.* **7**, eabf5676 (2021).